Mesoscale Properties of Clay Aggregates from Potential of Mean Force Representation of Interactions between Nanoplatelets

Davoud Ebrahimi[†], Andrew J. Whittle[†], Roland J.-M. Pellenq[†§‡,*]

[†]Department of Civil and Environmental Engineering

Massachusetts Institute of Technology, Cambridge, MA 02139, USA

[§]Centre Interdisciplinaire de Nanosciences de Marseille, Aix-Marseille Université,

CNRS, Campus de Luminy, 13288 Marseille Cedex 09, France

[‡] $<$ MSE $>^2$, UMI 3466 CNRS-MIT, Cambridge, MA 02139, USA

Abstract

Face-to-face and edge-to-edge free energy interactions of Wyoming Na-montmorillonite platelets were studied by calculating potential of mean force along their center to center reaction coordinate using explicit solvent (i.e., water) molecular dynamics and free energy perturbation methods. Using a series of configurations, the Gay-Berne potential was parametrized and used to examine the meso-scale aggregation and properties of platelets that are initially random oriented under isothermal-isobaric condition. Aggregates of clay was defined by geometrical analysis of face-to-face proximity of platelets with size distribution described by a log-normal function. The isotropy of the microstructure was assessed by computing a scalar order parameter. The number of platelets per aggregate and anisotropy of the microstructure both increases with platelet plan area. System becomes more ordered and aggregate size increases with increasing pressure until maximum ordered state. Further increase of pressure slides platelets relative to each other leading to smaller aggregate size. The geometrical arrangement of aggregates affects mechanical properties of the system. The elastic properties of the meso-scale aggregate assembly are reported. It is found that the elastic properties at this scale are close to the cubic systems. The elastic stiffness and

anisotropy of the assembly increases with the size of the platelets and the level of external pressure.

* Author to whom correspondence should be addressed. E-mail: pellenq@mit.edu.

Introduction

Clay is the most abundant mineral on the earth[1] and one of the most important industrial materials with a wide range of applications in construction, environmental, pharmaceutical and process industries.[2] Aggregation of clay mineral plays an important role in calculating the physical properties of soils such as elastic stiffness properties that control elastic wave propagation and the transport of ionic substances required for applications in waste management and environmental protection. Aggregation or dispersion of clay particles also affects the viscosity of drilling fluids. For these reasons, the coagulation of clay particles has received prominent attention in the literature.[3–13]

Clay minerals have a layered structure at the nanoscale. Each layer consists of some combinations of two sheet types with silicon tetrahedra and aluminum octahedra as basic units. For instance, the structure of natural Wyoming Na-montmorillonite has the following experimental formula[14]: $Na_{0.75}$ $nH_2O[Si_{7.75}Al_{0.25}][Al_{3.5}Mg_{0.5}]O_{20}(OH)_4$. This structure comprises two tetrahedral sheets sandwiching an octahedral sheet. Due to isomorphous substitutions of metal ions, the clay has a net negative surface charge. For the Wyoming Na-montmorillonite, 3.125% of the silicon ions, Si^{4+}, in the tetrahedral sheet are substituted by aluminum, Al^{3+}, while 12.5% of the aluminum ions, Al^{3+}, in the octahedral sheet are substituted by magnesium, Mg^{2+}. In the current research the negative charge is balanced by sodium ions, Na^{+1} between the clay layers. In a recent study[15], we characterized structural and mechanical properties of montmorillonite at the atomic scale. This paper presents a methodology to describe clay aggregates at the meso-scale from a simulation point of view.

The fundamental multi-scale approach toward the understanding clay behavior at the macroscopic scale (to address practical applications in geotechnical and petroleum engineering) aims at modeling the material at scales ranging from the atomistic level to the macroscopic system. Molecular dynamics simulation (MD) is a versatile technique to study interaction between colloidal nanoplatelets at the atomistic scale. In order to represent clay aggregates with mesopores and grain boundaries, the model must be scaled up from the atomistic level

to the submicron length scale. This exceeds the computational possibilities of full atomistic models and motivates a multiscale and consistent approach. Previous attempts to study clay aggregates were based on using quadrupoles[16,17] or pseudo charge sites to represent clay platelets.[18–25] The multipole representation of platelets might not be effective because of difficulties in modeling the charge distributions and existence of local defects associated with isomorphous substitutions. To overcome these limitations, we have used an upscaling strategy to run MD at meso-scale through calculation of free energy for face-to-face and edge-to-edge configurations of clay nanoplatelets using full atomistic representation of platelets, water molecules and ions. We then use the thermodynamic perturbation method to calculate the potential of mean force (PMF) (e.g. free energy) as a function of the distance between the centers of two platelets, an approach previously used for interaction between two graphene sheets.[26] The free energy is then used to calibrate the Gay-Berne (GB) potential[27] for different platelet sizes to study meso-scale interactions of multiple platelets with different orientations. The resulting arrangements of particles determine the microstructure of clay aggregates that control mechanical properties such as elastic stiffness. We characterize microstructure of the stabilized systems and report their full elastic properties.

Nano-scale PMF calculation

The proposed methodology begins with the calculation of the free energy along a reaction coordinate which corresponds to the separation distance (Figure 1) for face-to-face and edge-to-edge interactions of two Wyoming Na-montmorillonite platelets in liquid water. In order to calculate the change in free energy of the system from state A, when clay platelets are far from each other, to state B, when they are in close proximity, we define several intermediate states covering the change from state A to state B in small increments to enhance sampling of the phase space. Using stratification strategy, successive states are separated by low energy barriers such that the phase space is fully explored enabling statistical averaging of the

states.[28] We construct series of MD trajectories, each one representing one value of center to center distance. The trajectory of the MD simulation at one state is perturbed along the reaction coordinate to the target state while all other degrees of freedom are frozen. Free energy differences between two successive reference and target thermodynamic states will be calculated and added along the transformation path from state A to state B.

The analyses are carried out using the CLAYFF[29] force field that has been used successfully for simulation of clay minerals.[30,31] CLAYFF is a versatile force field built around the flexible version of the Simple Point Charge (SPC) water model.[32]

Full atomistic MD simulations were carried out by using the GROMACS[33] simulation package. The atomic structures were visualized using VMD[34] molecular graphic software.

The crystallography for 2:1 clay mineral was taken from Refson et al.[35] Isomorphous substitution was carried out randomly. We obeyed Lowenstein's rule for distribution of defects. Depending on the statistical ensemble, the Nosé–Hoover thermostat[36,37] is used to control temperature and the Parrinello–Rahman[38] barostat to control pressure in the system. An integration time step of 1 fs (femto second) was used in all full atomistic simulations. Three-dimensional, periodic boundary conditions were applied along with the minimum image convention (a cutoff radius of 8.5 Å was used for short range interactions). The long range electrostatic coulombic interactions were calculated using Particle Mesh Ewald summation.[39,40] Bond lengths and angles of the water molecules were constrained using the SHAKE algorithm[41] and clay platelets were kept frozen and rigid at each specific separation distance. The following sections summarizes the simulation details for edge-to-edge and face-to-face interactions.

Edge-to-edge

Two identical clay platelets were placed at center-to-center separations ranging from r_i=39.75-61.25 Å with an increment of 0.25 Å. Figure 1(a) shows the typical structure of the simulated system at one of the separation distances. From now on, each separation distance is called

one state, unless otherwise stated. We performed 87 separate simulations at 300 K in the canonical (NVT) ensemble. Each platelet consists of 4×4 unit cells with the longest dimension along y axis. Four edge sites on each side (along y) corresponding to [0 1 0] edges obtained by cutting the unit cell. Broken bonds were saturated with H or OH groups. Figure 1(b) shows the geometry of the edge sites taken from ab initio simulations of Churakov.[42,43] Edge corrections introduce $H_{32}O_{16}$ extra atoms on each platelet. The average length of the platelet in the y direction is ∼40 Å. We assigned a partial charge equal to 0.45e for a hydrogen atom on the edge (H) to keep the system neutral. Platelets are continuous in the x direction. The two platelets were solvated in the center of a rectangular box. The solvation process was performed by stacking equilibrated boxes of SPC water molecules[32] to form a rectangular box of 20.87 Å(x)×140 Å(y)×46.56 Å(z) containing 3882 water molecules which is constant for all states. Water molecules have been removed from the box if the distance between an atom in the water molecule and an atom in the clay structure is less than sum of their van der Waals radii. It has been shown that structure and dynamics of water molecules on the clay surface are only affected over two to three molecular layers from the surface.[44] In our simulations, the thickness of water phase on each side of the clay platelet or on each edge at the largest separation distance is about 20 Å corresponding to more than six molecular water layers (diameter of a water molecule ∼ 3 Å). As a result, the interaction of two clay platelets (edge-to-edge or face-to-face) separated by water layers with 40 Å thickness is efficiently shielded to have no interaction between a platelet and its image. Moreover, the simulation box is large enough so that properties of water molecules near to the boundaries of the box approximate closely to those of bulk water. After solvation, each system was equilibrated for 0.5 ns (nano second). Free energy differences between successive states are calculated over a 2.5 ns production period. Each state, r_i, was perturbed in two directions: forward and reverse, $r_{i\pm1}=r_i\pm dr_i$ where dr_i=0.25 Å (except for the end states which perturbed in one direction only). Following Zwanzig[45], the free energy difference between the reference

state, r_i, and target state, $r_{i\pm1}$, can be calculated using free energy perturbation theory:

$$\Delta G(r_i \rightarrow r_{i\pm1}) = G(r_{i\pm1}) - G(r_i) = -\frac{1}{\beta} \ln \langle exp\left(-\beta \Delta U\right) \rangle_i \tag{1}$$

$\Delta U = U(r_{i\pm1}) - U(r_i)$ and $\beta = (k_B\ T)^{-1}$ where T is the temperature, k_B is Boltzmann's constant and U denotes the potential energy of the system. The brackets denote canonical ensemble average over the trajectory and subscript i indicates that the average is taken in the reference state. We calculated 172 free energy differences between successive states. In order to eliminate systematic sampling bias due to exponential averaging we used simple overlap sampling (SOS) of the forward and reverse perturbation as an estimate of ΔG[28,46]:

$$\Delta G(r_i \rightarrow r_{i\pm1}) = -\frac{1}{\beta} \ln \left[\frac{\langle exp\left(-\beta \Delta U/2\right) \rangle_i}{\langle exp\left(\beta \Delta U/2\right) \rangle_{i+1}} \right] \tag{2}$$

The total potential of mean force at each separation distance (r=r_i) was calculated by sequentially summing up all the free energy changes from the largest separation (r=61.25 Å) to that state (r=r_i) assuming zero value for the free energy of the system at the largest separation (r=61.25 Å). Figure 2(a) shows the potential of the mean force for edge-to-edge interactions calculated over the range of states for selected analysis production periods. The results converge after averaging over 2.5 ns (i.e., 3 ns simulation and perturbation for each MD state). The PMF shows an oscillatory behavior with distance between energy minimums (or plateau) reflecting size of a water molecule (∼3 Å). In other words, rearrangement of the water molecules determines favorable positions of the clay platelets. As platelets come closer to each other, system crosses energy barriers to reach to the lowest free energy at r=45.5 Å. For r<45.5 Å, repulsion dominates the interaction of platelets indicating work needed to remove water molecules and bring platelets close together. Figure 2(b) shows PMF per unit length of the platelet which will subsequently be scaled for different platelet sizes (assuming 'D' as diameter of the platelet, values of the 'x' axis are modified to 'new r_i = old r_i -40 Å + D' and values of the 'y' axis are multiplied by the diameter of the platelet).

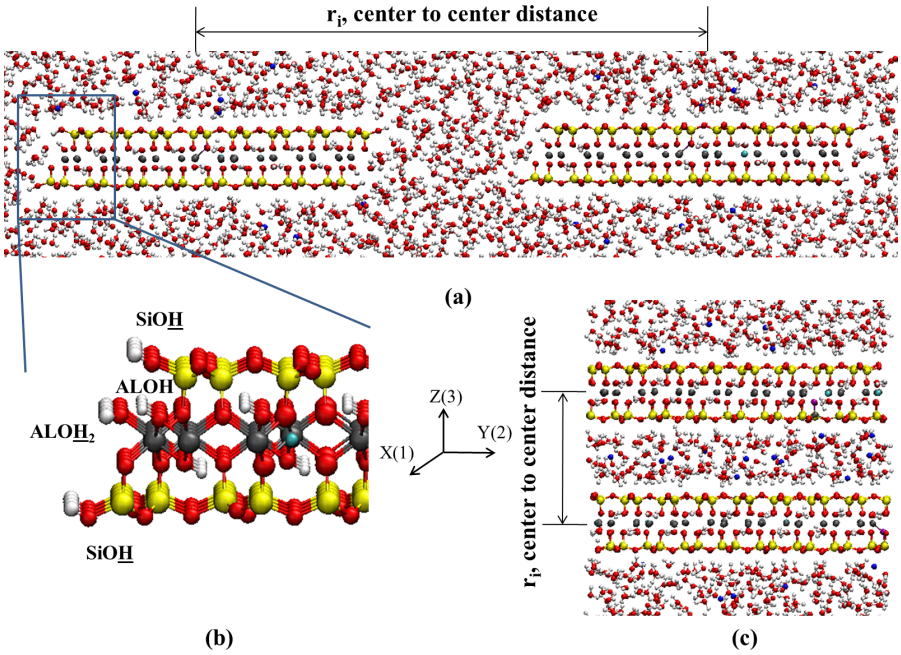

Figure 1: (a) Part of the typical simulation setup for studying edge-to-edge interaction (red, O; white, H; yellow, Si; grey, Al; cyan, Mg; blue, Na). (b) Detail of the edge [0 1 0] structure. Si tetrahedra end with an SiO<u>H</u> bond (top and bottom). Al octahedra end with AlOH inside the clay platelet and AlO<u>H</u>$_2$ on the broken edge. (c) Part of the typical simulation setup for studying face-to-face interaction

.

Face-to-face

Two identical clay platelets were placed at center to center separations of r_i=9.23-18.47 Å with an increment of 0.25 Å. Figure 1(c) shows the typical structure of the simulated system in one of the separation distances. Platelets are continuous in x and y directions. We performed 38 separate simulations at T=300 K in the canonical (NVT) ensemble. Table 1 summarizes the distribution of water molecules between the platelets (I) and outside (O). In order to create structures with different amount of water between clay platelets, we displaced them to put different number of water molecules in between and the rest outside. Then for each state, we ran a 2 ns (NPT) simulation. Initial states of each (NVT) simulation was taken from trajectories of (NPT) simulations. Each platelet consists of 4×4 unit cells with the longest dimension along y axis. In order to be consistent with edge-to-edge simulations, we put 3882+2×16 (taking into account extra H and OH due to edge corrections)=3914

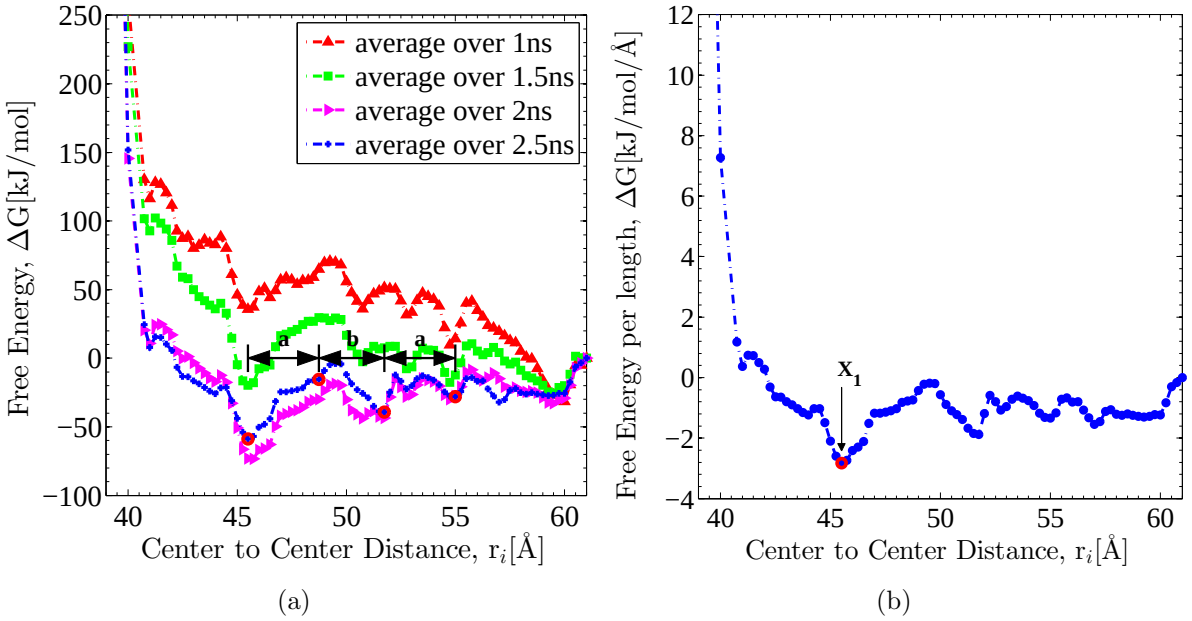

Figure 2: Potential of mean force for edge-to-edge interaction of clay platelets. (a) total PMF, a,b = 3.25, 3 Å , respectively. (b) PMF per length.

water molecules in each system. The initial dimension of the rectangular box in each (NPT) simulation was 20.87 Å(x)×36.31 Å(y)×179.62 Å(z). The average final dimensions of the system were 20.72 Å(x)×36.05 Å(y)×179.07 Å(z). From this point, each (NVT) simulation was equilibrated for 0.5 ns. Free energy difference between successive states was calculated from a 3 ns production period. Each state was perturbed in two directions to create 74 perturbed states. The energy differences between successive states are then reported using the SOS method (Equation(2)). Total potential of mean force at each separation distance (r=r_i) was calculated by sequentially summing up all the free energy changes from the largest separation (r=18.47 Å) to the state of interest (r=r_i) assuming zero value for the free energy of the system at largest separation (r=18.47 Å).

Free energy for face-to-face interaction of clay platelets for different lengths of MD trajectory are shown in Figure 3(a). The calculated free energy converges after averaging over 3 ns (3.5 ns MD simulation). Similar to edge-to-edge interaction, local minima of the free energy curve are separated by distances comparable to the diameter of a water molecule. This is in agreement with previous studies reporting oscillatory changes in the interaction between two

Table 1: Center to center distances (r_i) and number of water molecules (N_w) inbetween (I) and outside (O) of the clay platelets for each state.

		N_w				N_w				N_w	
state	$r_i[\AA]$	I	O	state	$r_i[\AA]$	I	O	state	$r_i[\AA]$	I	O
1	9.23	0	3914	14	12.49	79	3835	27	15.74	159	3755
2	9.48	4	3910	15	12.74	80	3834	28	15.99	174	3740
3	9.74	7	3907	16	12.99	87	3827	29	16.24	177	3737
4	9.99	7	3907	17	13.24	93	3821	30	16.49	178	3736
5	10.24	7	3907	18	13.49	101	3813	31	16.72	178	3736
6	10.49	8	3906	19	13.74	108	3806	32	16.97	179	3735
7	10.74	8	3906	20	13.99	112	3802	33	17.22	179	3735
8	10.99	14	3900	21	14.24	113	3801	34	17.47	179	3735
9	11.24	18	3896	22	14.49	116	3798	35	17.72	197	3717
10	11.49	24	3890	23	14.74	118	3796	36	17.97	210	3704
11	11.74	32	3882	24	14.99	119	3795	37	18.22	228	3686
12	11.99	42	3872	25	15.24	130	3784	38	18.47	232	3682
13	12.24	54	3860	26	15.49	148	3766				

surfaces with periodicity corresponding to the diameter of a water molecule.[47–49] To have particles approach each other and reach the minimum free energy around 11 Å, they should overcome energy barriers at larger distances. Due to large repulsive interactions at smaller distances (r<11 Å), removing more water molecules is not favorable for the system. This is an indication of the existence of some bonded water molecules which cannot be removed easily. This is consistent with the experimental measurements using infrared spectroscopy.[50–54] Figure 3(b) shows PMF for face-to-face interactions per surface area which will be scaled for different platelet sizes (values of the 'y' axis are multiplied by the surface area of the platelet).

Meso-scale: Gay-Berne Potential

The meso-scale simulations are based on the Gay-Berne (GB)[27] potential as implemented[55] in LAMMPS code.[56] The GB potential is a single site potential used for interaction of two

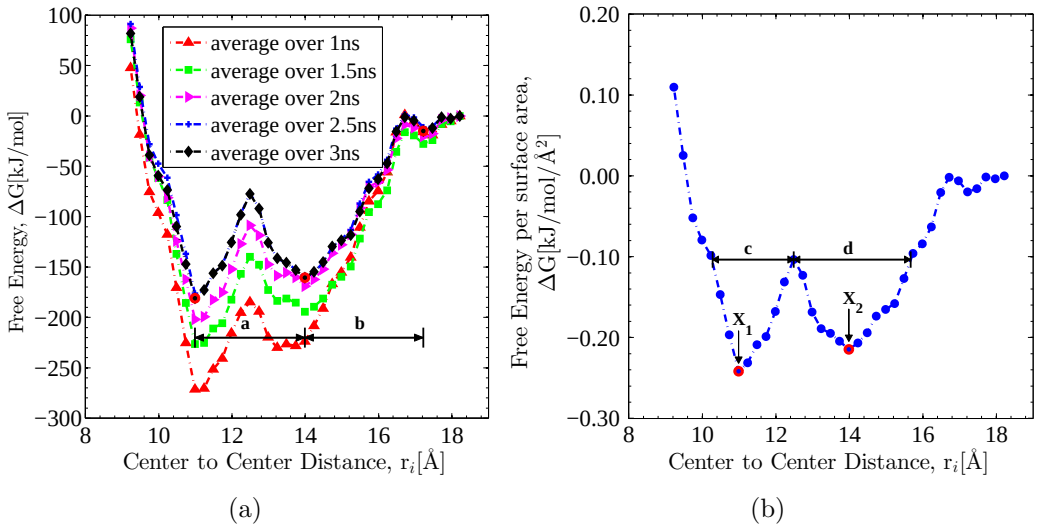

Figure 3: Potential of mean force for face-to-face interaction of clay platelets. (a) total PMF, a,b = 3, 3.22 Å , respectively. (b) PMF per surface area. Width of the second energy well is wider than the first one (i.e., d>c).

rigid, aspherical, ellipsoidal particles. As we know from electron microscopy, platelets of clay are approximately equidimentional in plan.[57] Moreover, analysis by atomic force microscopy shows that an ellipsoidal (oblate) geometry is a reasonable approximation for describing the clay platelets.[58] Here, we treat each platelet of clay as an effective ellipsoidal GB particle. GB was originally developed for similar ellipsoidal particles and then generalized for dissimilar biaxial particles.[59] Using the notations of Everaers and Ejtehadi,[60] the GB potential can be written as:

$$U = 4\epsilon \left[\left(\frac{\sigma}{h_{12} + \sigma} \right)^{12} - \left(\frac{\sigma}{h_{12} + \sigma} \right)^{6} \right] . \eta_{12} . \chi_{12} \tag{3}$$

In the first term which is similar to Lennard-Jones potential, ϵ determines the energy scale, σ is the atomic interaction radius and function h_{12} approximates anisotropic interparticle distance:

$$h_{12} = r - \sigma_{12} \tag{4}$$

And:

$$\sigma_{12} = \left(\frac{1}{2} \hat{\mathbf{r}}_{\mathbf{12}}^{T} \mathbf{G}_{\mathbf{12}}^{-\mathbf{1}} \hat{\mathbf{r}}_{\mathbf{12}} \right)^{-\mathbf{1/2}} \tag{5}$$

Where $\mathbf{r_{12}} = \mathbf{r_2} - \mathbf{r_1} = \mathrm{r}\ \hat{\mathbf{r}}_{\mathbf{12}}$ is the center to center separation vector, r is center to center distance, $\hat{\mathbf{r}}_{\mathbf{12}}$ is the unit vector and:

$$\mathbf{G_{12}} = \mathbf{A}_1^T \mathbf{S}_1^2 \mathbf{A}_1 + \mathbf{A}_2^T \mathbf{S}_2^2 \mathbf{A}_2 \tag{6}$$

Where $\mathbf{S_i} = \mathrm{diag}(a_i, b_i, c_i)$ is shape matrix which is defined by three radii a_i, b_i, c_i. $\mathbf{A}_i$ represents rotation matrix which defines transformation of each particle from local frame to global frame. The second term characterizes anisotropic interaction of particles due to their shapes:

$$\eta_{12} = \left[\frac{2 s_1 s_2}{\det(\mathbf{G_{12}})} \right]^{1/2} \tag{7}$$

And:

$$s_i = \left[a_i b_i + c_i c_i \right] \left[a_i b_i \right]^{1/2} \tag{8}$$

The third term characterizes anisotropic interaction of particles based on relative free energy well depths of edge-to-edge and face-to-face interactions:

$$\chi_{12} = \left(2 \hat{\mathbf{r}}_{\mathbf{12}}^T \mathbf{B}_{\mathbf{12}}^{-\mathbf{1}} \hat{\mathbf{r}}_{\mathbf{12}} \right)^{\mathbf{2}} \tag{9}$$

With:

$$\mathbf{B_{12}} = \mathbf{A}_1^T \mathbf{E}_1 \mathbf{A}_1 + \mathbf{A}_2^T \mathbf{E}_2 \mathbf{A}_2 \tag{10}$$

Where $\mathbf{E_i} = \mathrm{diag}(\epsilon_{ia}, \epsilon_{ib}, \epsilon_{ic})$ is the energy matrix which is defined by relative well depths of edge-to-edge and face-to-face interactions. In summary, in order to define interactions between two disc-like platelets (same x and y dimensions) we need to specify five parameters: $\mathbf{x} = \{a(b), c, \sigma, \epsilon_a(\epsilon_b), \epsilon_c\}$, two shape parameters $a(= b), c$ (with length dimension), one interaction distance parameter σ (with length dimension) and two energy parameters per particle, $\epsilon_a(= \epsilon_b), \epsilon_c$ which are dimensionless. These parameters are adjusted by fitting Equation(3) to edge-to-edge and face-to-face interactions of two platelets. Following Berardi et al.[61], we

defined a cost function and optimized characteristic features (Figure 4) of edge-to-edge and face-to-face energy profiles to find parameters of GB potential:

(1) The well depth, $P_1^{GB} = -\epsilon \,.\, \eta_{12} \,.\, \chi_{12}$

(2) The separation distance corresponding to the well minimum, $P_2^{GB} = \sigma_{12} + \sigma(2^{1/6} - 1)$

(3) The soft contact distance, $P_3^{GB} = \sigma_{12}$

(4) Characteristic width of the potential energy well (at half depth),

$P_4^{GB} = \sigma \left[\left(4 + 2\sqrt{2}\right)^{1/6} - \left(4 - 2\sqrt{2}\right)^{1/6} \right]$

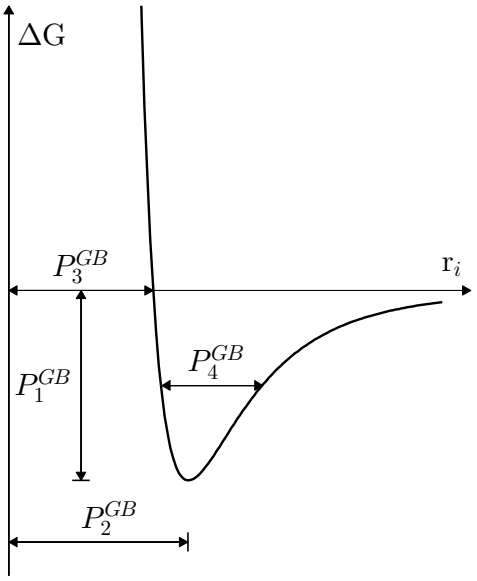

Figure 4: Fitting parameters of the GB potential.

The following cost function was used in fitting procedure:

$$\Omega(\mathbf{x}) = \frac{1}{4N_c} \sum_{N_c} \sum_{i=1}^{4} \left(\frac{P_i^{GB} - P_i^{CLAYFF}}{N_i^f} \right)^2 \tag{11}$$

Superscript $CLAYFF$ denotes corresponding value from full atomistic simulation. N_c is the number of arrangements (here N_c=2 as we are fitting to face-to-face and edge-to-edge interactions) and N_i^f is normalizing factor.

For $i = 1$, $N_i^f = P_1^{CLAYFF}$, well depth for face-to-face interaction. For $i = 2, 3, 4$, $N_i^f =$

P_2^{CLAYFF}, distance of well minimum for edge-to-edge interaction.

We parametrized the GB potential for three different platelet sizes : 100 Å, 500 Å and 1000 Å. In all those the GB potential was fitted to the main (first) free energy minimum (X_1, Figures 2(b) and 3(b)) denoted by '$\triangledown$' (P=1 atm), '$\blacktriangledown$' (P=10 atm), '$\blacktriangledown\!\!/$' (P=50 atm), '$\blacktriangledown\!\!/\!\!/$' (P=300 atm) and '$\blacktriangledown\!\!/\!\!/\!\!/$' (P=800 atm). A second set of GB parameters was chosen for the 1000 Å platelet by fitting to the second free energy minimum of the face-to-face interaction (X_2, Figure 3(b)) denoted by '$\triangledown\triangledown$' and the main (first) minimum of edge-to-edge interaction (X_1, Figure 2(b)). Figures 5(a), (b), (c) and (d) show fitted GB to full atomistic simulations for D= $\overset{\triangledown}{1}00$, $5\overset{\triangledown}{0}0$, $10\overset{\triangledown}{0}0$($\overset{\blacktriangledown}{1}000$,$\overset{\blacktriangledown\!\!/}{1}000$,$\overset{\blacktriangledown\!\!/\!\!/}{1}000$,$\overset{\blacktriangledown\!\!/\!\!/\!\!/}{1}000$), and $\overset{\triangledown\triangledown}{1}000$ Å. The GB parameters for different cases are listed in Table 2. By increasing diameter of the platelet, potential wells become deeper due to larger edge and surface. Moreover, difference between face-to-face and edge-to-edge interaction increases since face-to-face free energy scales with (length)^2 while edge-to-edge interaction scales with (length). This is reflected in the change of energy parameters (ϵ_a(ϵ_b) and ϵ_c Table 2).

For each case, ten different samples were prepared with initial random orientation of particles by putting 1000 platelets in a simple cubic lattice with interatomic spacing of (r_a) larger than diameter of a platelet. For each sample, an NPT simulation was performed at constant temperature, T=300 K to find the final 'jamming state' configuration which is characterized by no further change in potential energy of the system. Figure 6 shows step function of applied pressure in those simulations. Table 3 lists details of the simulations for each size of platelets. The Nosé–Hoover thermostat[36,37] is used to control temperature and the Parrinello–Rahman[38] barostat to control pressure in the system. The pressure and temperature damping parameters were 1 ns and 0.001 ns, respectively. For each column, ten simulations were performed to sample phase space and report average properties of the final state. Initial state of each sample with P >1 was taken from the end of $10\overset{\triangledown}{0}0$ simulations (with P=1 atm).

Table 2: Parameter values of the GB potential.

	GB calibration case			
	$100^{\triangledown}$	$500^{\triangledown}$	$1000^{\triangledown}$,$1000^{\blacktriangledown}$,$1000^{\blacktriangledown/}$,$1000^{\blacktriangledown//}$,$1000^{\blacktriangledown///}$	$1000^{\triangledown\triangledown}$
2a,2b(Å)	104.12	504.12	1004.12	1004.05
2c(Å)	9.62	9.62	9.62	12.25
σ(Å)	11.00	11.00	11.00	14.00
ϵ_a, ϵ_b	12.37	12.88	12.94	16.47
ϵ_c	105.99	551.81	1108.46	1252.60

$\triangledown$: P=1 atm, $\blacktriangledown$: P=10 atm , $\blacktriangledown/$: P=50 atm , $\blacktriangledown//$: P=300 atm , $\blacktriangledown///$: P=800 atm , $\triangledown\triangledown$: P=1 atm and GB fitted to the second minimum of face-to-face interaction

Table 3: Details of simulations performed in NPT (T=300 K) ensemble for different systems at meso-scale. dt: time step, r_a: initial interatomic spacing, r_c: cutoff radius. Symbols as in Table 2.

	GB calibration case							
	$100^{\triangledown}$	$500^{\triangledown}$	$1000^{\triangledown}$	$1000^{\triangledown\triangledown}$	$1000^{\blacktriangledown}$	$1000^{\blacktriangledown/}$	$1000^{\blacktriangledown//}$	$1000^{\blacktriangledown///}$
dt(fs)	40	40	40	40	40	40	40	40
r_a, r_c(Å)	120	520	1020	1020	1020	1020	1020	1020
p_0(atm)	0	0	0	0	1	1	1	1
p_1(atm)	1	1	1	1	10	50	300	800
t_1(ns)	40	40	40	40	120	120	120	120
t_f(ns)	5000	1200	1200	1200	360	320	240	200

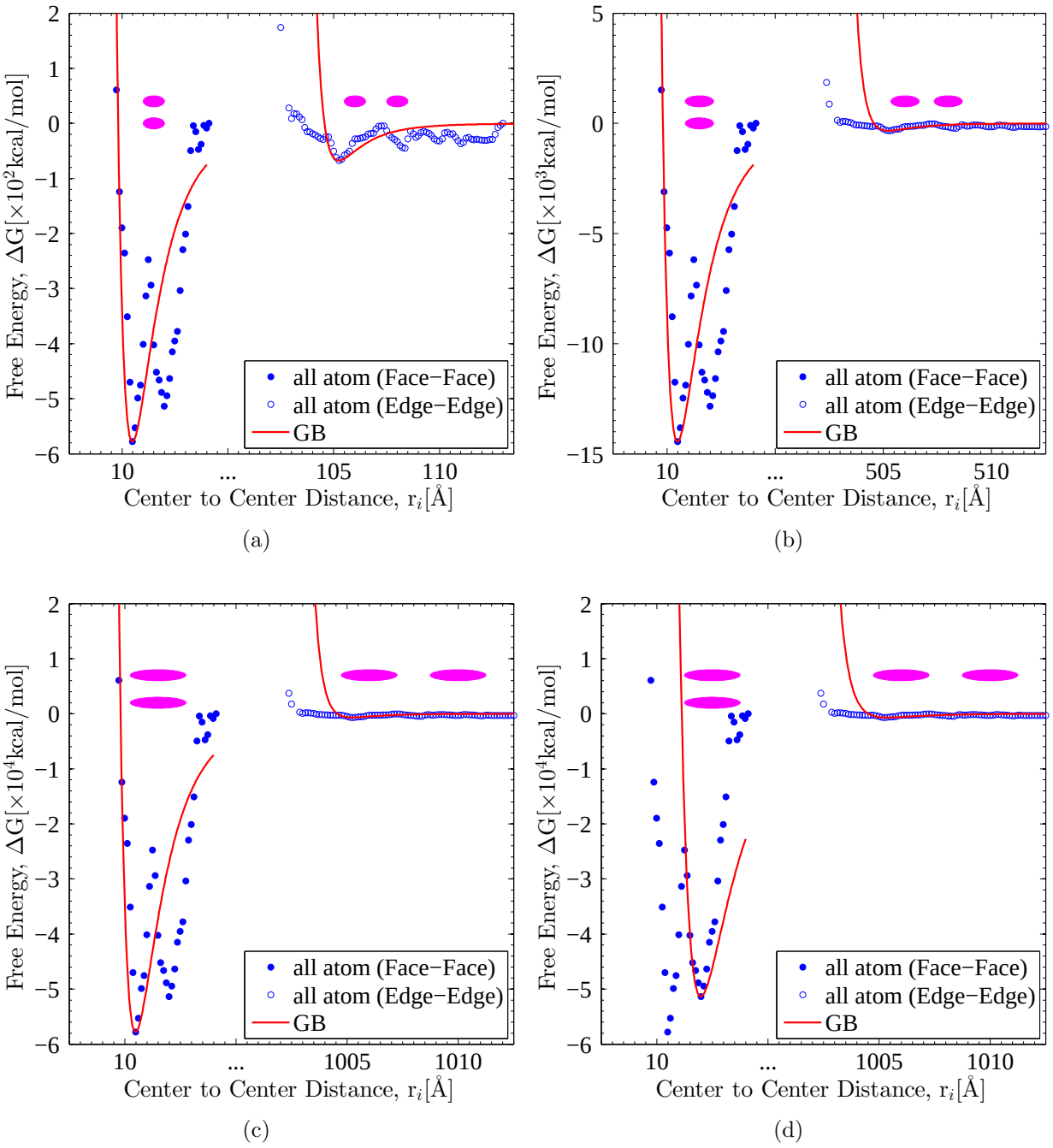

Figure 5: Fitting GB potential to face-to-face and edge-to-edge interactions for different platelet diameters, D (a) D=$\overset{\triangledown}{1}00$ Å (b) D=$\overset{\triangledown}{5}00$ Å (c) D=$\overset{\triangledown}{1}000$,$1\overset{\blacktriangledown}{0}00$,$1\overset{\blacktriangledown\prime}{0}00$,$1\overset{\blacktriangledown\prime\prime}{0}00$,$1\overset{\blacktriangledown\prime\prime\prime}{0}00$ Å, fitted to the first well of face-to-face interaction. (d) D=$\overset{\triangledown\triangledown}{1}000$ Å, fitted to the second well of face-to-face interaction ("$\cdots$" denotes contraction of the x scale).

Meso-scale Aggregation

The meso-scale aggregation of clay platelets can be examined by considering snapshots of the simulation at selected timesteps using QMGA[62] molecular graphics software. Each

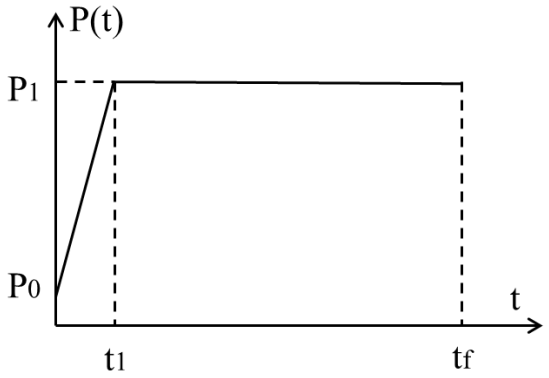

Figure 6: Step function of applied pressure, p(t), in NPT simulations.

simulation, uses a total number of 1000 equal-sized clay platelets with random orientations in a unit cell with different GB calibrations for different particle sizes and confining pressures (Table 3). Geometrical and mechanical properties are averaged over ten samples for each type of simulation. A qualitative picture of the evolution of the system of particles during MD simulations for a typical sample can be seen in Figure 7. This example shows snapshots of a sample $1\overset{\triangledown}{0}00$ GB case (i.e., platelets of diameter 1000 Å at P=1 atm and T=300 K). Platelets are color coded based on the orientation of their normal vector with respect to the Z axis (ϕ angle). When platelets become clustered into aggregates, their normal vectors point in the same direction and the spectrum of colors decreases with time as the sample compresses to the fully jammed configuration (t=1200 ns, Figure 7(c)). In this case, Figure 8(a) shows that there are no further changes in the total energy of the system for t$\geqslant$1000 ns ($1\overset{\triangledown}{0}00$ case). Figure 9 shows that systems with smaller platelets have larger kinetic energy compared to the total energy scale. For instance, the percentage of kinetic energy to total energy decreases from 0.25% to 0.0026% as size of the platelet increases from 100 Å to 1000 Å. In other words, temperature becomes irrelevant which is characteristic of the jamming state. Smaller particles need longer simulation times to reach to their final jammed state as seen in Figure 8(b) for a $1\overset{\triangledown}{0}0$ Å simulation case. In this example the final state is attained at t$\sim$5000 ns.

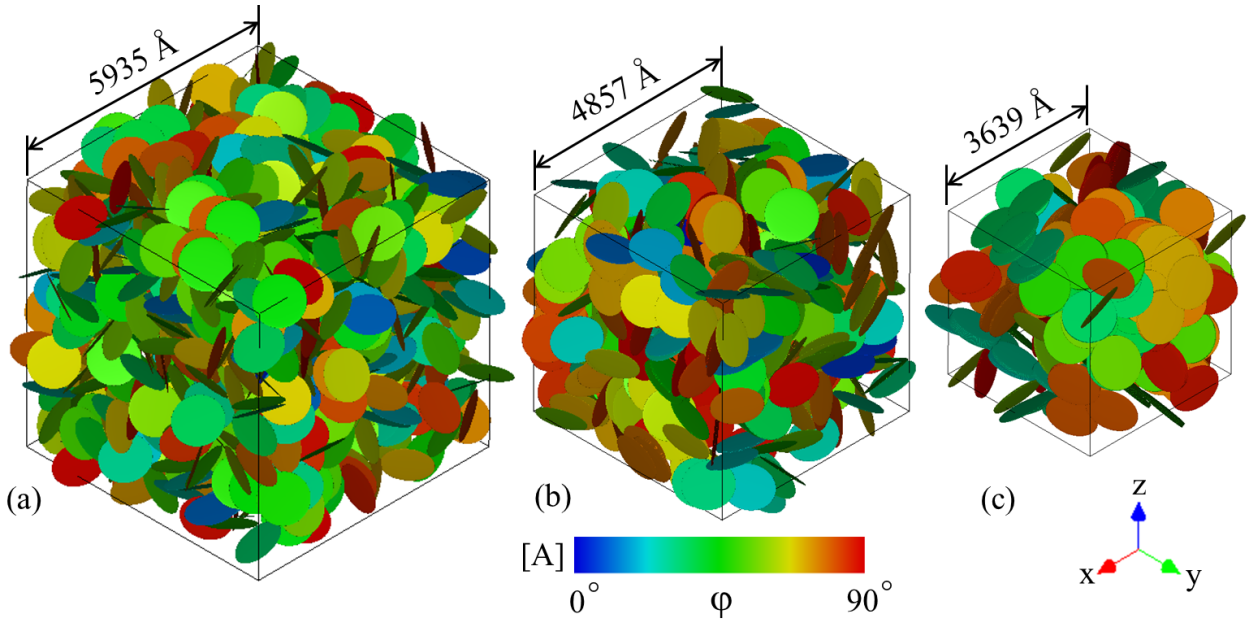

Figure 7: Snapshots showing aggregation of 1000̊ Å simulation at: (a) t=40 ns (b) t=200 ns (c) t=1200 ns. The particles orientations are color coded according to the ϕ angle, orientation of their normal vector with respect to the Z axis (colorbar A).

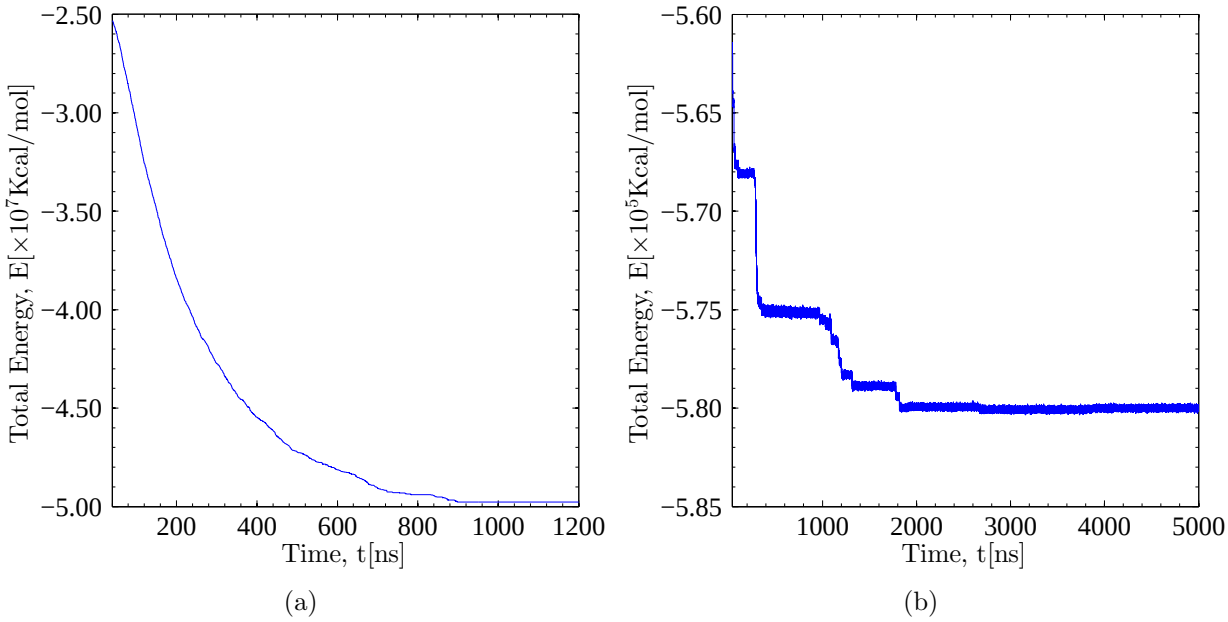

Figure 8: Total energy of the system of platelets for typical samples from simulations (see Table 3) (a) 1000̊ Å (b) 100̊ Å .

Geometrical analysis

Following Chen et al.[63], we used two criteria to determine whether two platelets are stacked on top of each other. Figure 10 shows the two criteria used for the analysis of platelets

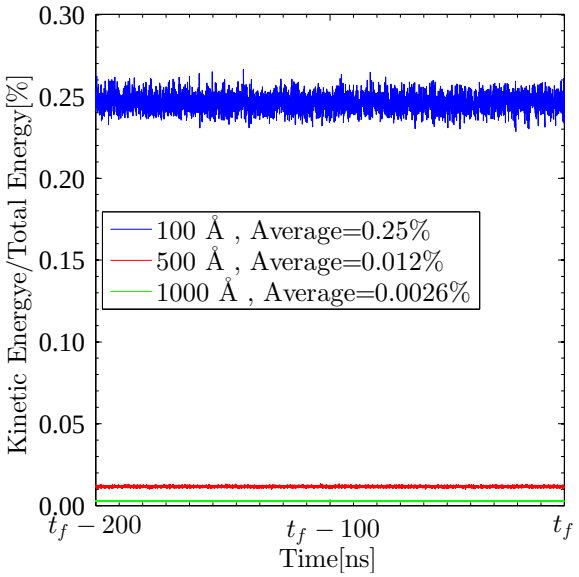

Figure 9: Percentage of kinetic energy to total energy in the last 200 ns of simulation for typical samples (see Table 3).

stacking. Two platelets are assumed to belong to the same clay aggregate (stack) if :

(a) their interlayer distance, r, is less than an upper limit, r_u. The current analysis assumes that r_u is 25% larger than the equilibrium distance for face-to-face interactions to allow for offsetting of platelets. For seven of the GB calibration cases ($\overset{\triangledown}{1}00$, $5\overset{\triangledown}{0}0$, $10\overset{\triangledown}{0}0$, $10\overset{\blacktriangledown}{0}0$, $10\overset{\blacktriangledown\prime}{0}0$,$10\overset{\blacktriangledown\prime\prime}{0}0$ and $10\overset{\blacktriangledown\prime\prime\prime}{0}0$ Å), r_u=13.75 Å; while r_u=17.5 Å for $10\overset{\triangledown\triangledown}{0}0$ Å.

(b) the absolute value of scalar product of the two normal vectors of the platelets is greater than 0.95 ($n_1.\ n_2 > 0.95$).

Figures 11 and 12 illustrate probability distribution of aggregate stack sizes averaged over ten simulations and fitted to log-normal distribution functions for GB cases with P=1 atm and P >1 atm, respectively. Log-normal distribution of stack sizes was reported in X-ray diffraction (XRD) and transmission electron microscopy (TEM) of Na-smectite.[64] In each case the goodness of fit is assesed using the chi-squared χ^2 test (see Table 4), at $\chi^2_{0.05} = 0.05$ significance level. The histograms of stack sizes were grouped into n_{bins}=10-14 centered on integer number of stacks. The last bins in the right tail of the distribution were merged together until the count in the extreme bin is at least 5. Degrees of freedom of the test, dof=n_{bins}-3 to take into account the two estimated parameters of the test, (μ,σ).

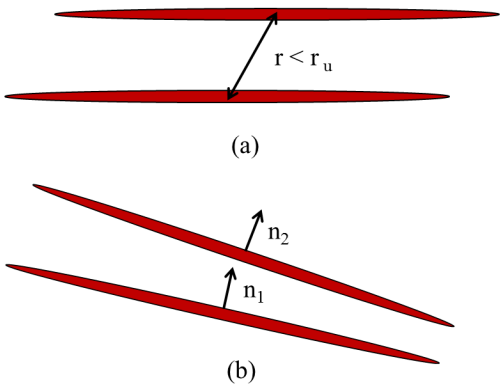

Figure 10: Criteria used for analysis of aggregation. (a) distance criterion (b) orientation criterion.

In all cases $\chi^2 < \chi^2_{0.05}$ which confirms that the log-normal distribution is able to represent the distribution of stack sizes at $\alpha = 0.05$ significance level. The average stack size (n) increases from 3.05 to 5.01 for platelets with size increasing from $\overset{\triangledown}{1}00$ Å to $\overset{\triangledown}{1}0\overset{\triangledown}{0}0$ Å (Table 4). This is in agreement with small angle X-ray scattering (SAXS) experiments of Segad et al.[65] who reported an increase in size of aggregates with increase in the platelet size for Ca-montmorillonite. As the surface area of a platelet increases the number of platelets subtended in its solid angle also increases. This means that each platelet would interact with many more other platelets. Moreover, since the interaction energy scales with the surface area, the attraction force between platelets increases which results in larger stack sizes. Increasing pressure from 1 atm to 10 atm ($1\overset{\triangledown}{0}0\overset{\triangledown}{0}$ vs $1\overset{\blacktriangledown}{0}0\overset{\blacktriangledown}{0}$, see Table 4) has similar effect with the average size of the aggregates increasing from 5.01 to 7.07. Figures 13 and 14 show typical equilibrated systems of platelets for samples with P=1 atm and P >1 atm, respectively. The effect of increase in pressure can be seen by comparing Figures 13(c) and 14(a) ($1\overset{\triangledown}{0}0\overset{\triangledown}{0}$ vs $1\overset{\blacktriangledown}{0}0\overset{\blacktriangledown}{0}$). However, fitting GB to the first or second potential energy well for face-to-face interaction, has no effect on the size of the aggregates ($1\overset{\triangledown}{0}0\overset{\triangledown}{0}$ vs $1\overset{\triangledown\triangledown}{0}0\overset{\triangledown\triangledown}{0}$, see Table 4). By increasing pressure to 50 atm, average stack size increases to 8.33. More increase in pressure results in decrease of the stack size (from 8.33 to 6.68 and 4.46 as pressure increases from 50 atm to 300 atm and 800 atm, respectively). This is due to the sliding of the platelets (more than r_u). We can see sliding of platelets from Figure 14(a) to Figure

Table 4: Results of geometrical analysis of aggregates. Symbols as in Table 2.

	GB calibration case							
	$\overset{\triangledown}{100}$	$\overset{\triangledown}{500}$	$\overset{\triangledown}{1000}$	$\overset{\triangledown\triangledown}{1000}$	$\overset{\blacktriangledown}{1000}$	$\overset{\blacktriangledown\prime}{1000}$	$\overset{\blacktriangledown\prime\prime}{1000}$	$\overset{\blacktriangledown\prime\prime\prime}{1000}$
n_{bins}	10	10	13	13	13	14	14	13
dof	7	7	10	10	10	11	11	10
χ^2	4.16	4.16	8.33	8.13	2.86	7.90	17.07	11.90
$\chi^2_{0.05}$	14.06	14.06	18.30	18.30	18.30	19.67	19.67	18.30
(μ,σ)	(0.94,0.59)	(1.01,0.62)	(1.38,0.68)	(1.38,0.68)	(1.69,0.73)	(1.80,0.80)	(1.26,1.13)	(0.89,1.10)
n	3.05	3.33	5.01	5.01	7.07	8.33	6.68	4.46
S	0.11±0.03	0.10±0.04	0.23±0.08	0.21±0.05	0.46±0.12	0.65±0.10	0.65±0.13	0.67±0.17

14(d). The same effect is reflected in the stack size distributions in Figure 12. By increasing pressure, distribution is skewed more to the left and number of isolated platelets increases. As a result, average number of platelets per stack decreases. Using transmission electron microscopy, scanning electron microscopy, SAXS and X-ray diffraction experiments[64,66–69] on different types of Na-smectites have found that particles typically comprise three to ten layers of platelets, consistent with our numerical simulations.

In order to study the degree of orientation of particles, we use a scalar measure of the orientation as an order parameter:

$$S = \left\langle \frac{3\,\cos^2\theta - 1}{2} \right\rangle \tag{12}$$

Where θ is the angle of normal vector of a platelet ($\mathbf{u}$) with director of the system ($\mathbf{n}$). The brackets denote average over all the particles. The director vector of a system of particles, ($\mathbf{n}$), is a measure of the average orientation of the particles in the system. Director is the eigenvector corresponding to biggest absolute eigenvalue of the order tensor, q_{ij} :

$$q_{ij} = \frac{1}{N}\sum_{m=1}^{N}\left(u_i u_j - \frac{1}{3}\delta_{ij}\right) \tag{13}$$

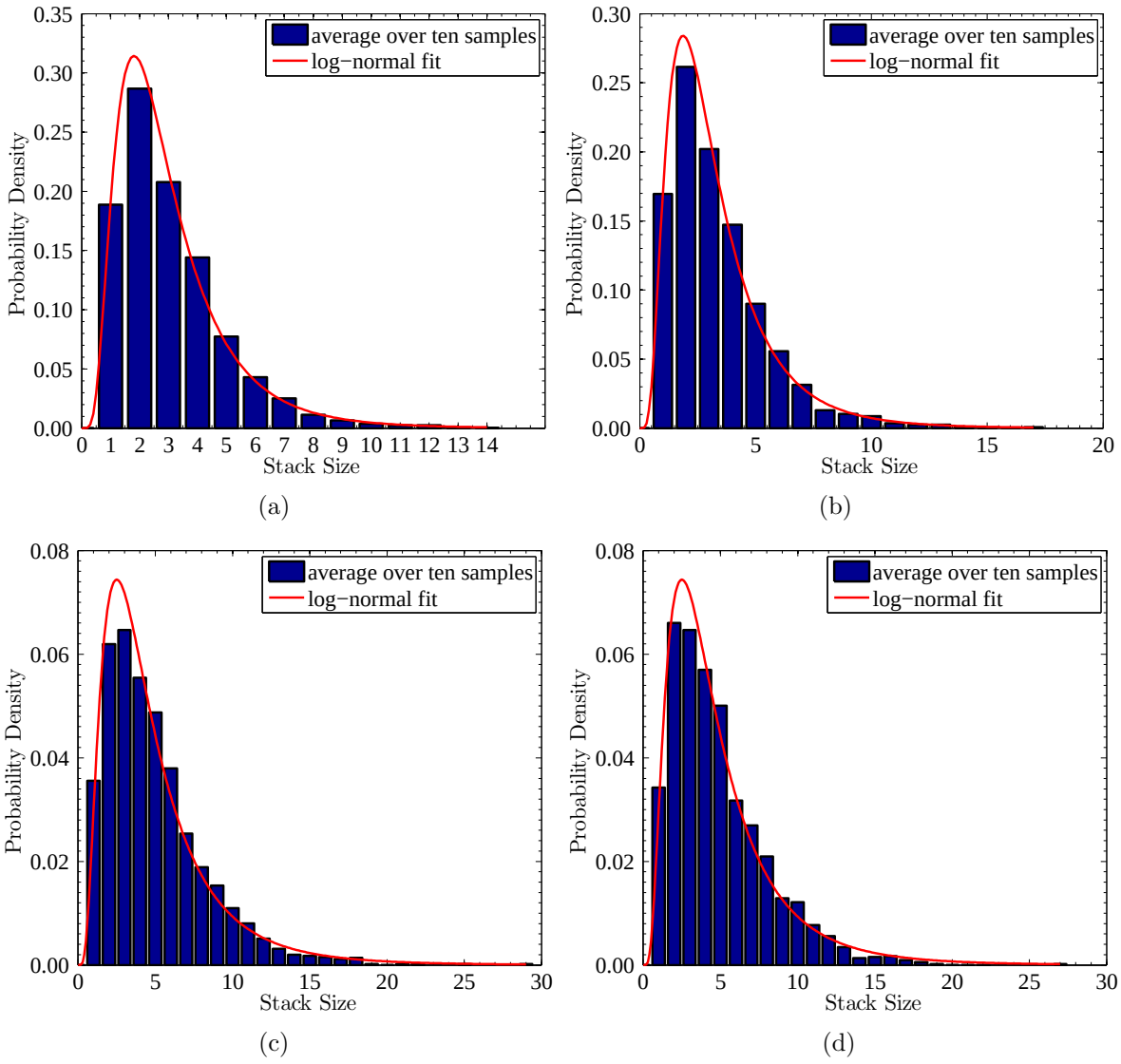

Figure 11: Probability distributions and fitted log-normal distributions to the stack size analysis for different types of simulations (P=1 atm, see Table 3): (a) $\overset{\triangledown}{1}00$ Å (b) $\overset{\triangledown}{5}00$ Å (c) $\overset{\triangledown}{1}000$ Å (d) $\overset{\triangledown\triangledown}{1}000$ Å

Where N is the number of particles and δ_{ij} is the Kronecker delta function. For completely isotropic and randomly oriented system S=0, while perfectly aligned systems have S=1. Results of the calculated order parameter are listed in the Table 4. As the size of the platelets increases from 100 Å to 500 Å there is little change in the order parameter of the particles (from 0.11 to 0.10 for $\overset{\triangledown}{1}00$ and $\overset{\triangledown}{5}00$, respectively). Similarly, fitting to the first or second potential energy well of the face-to-face interaction has little effect on S (from 0.23 to 0.21

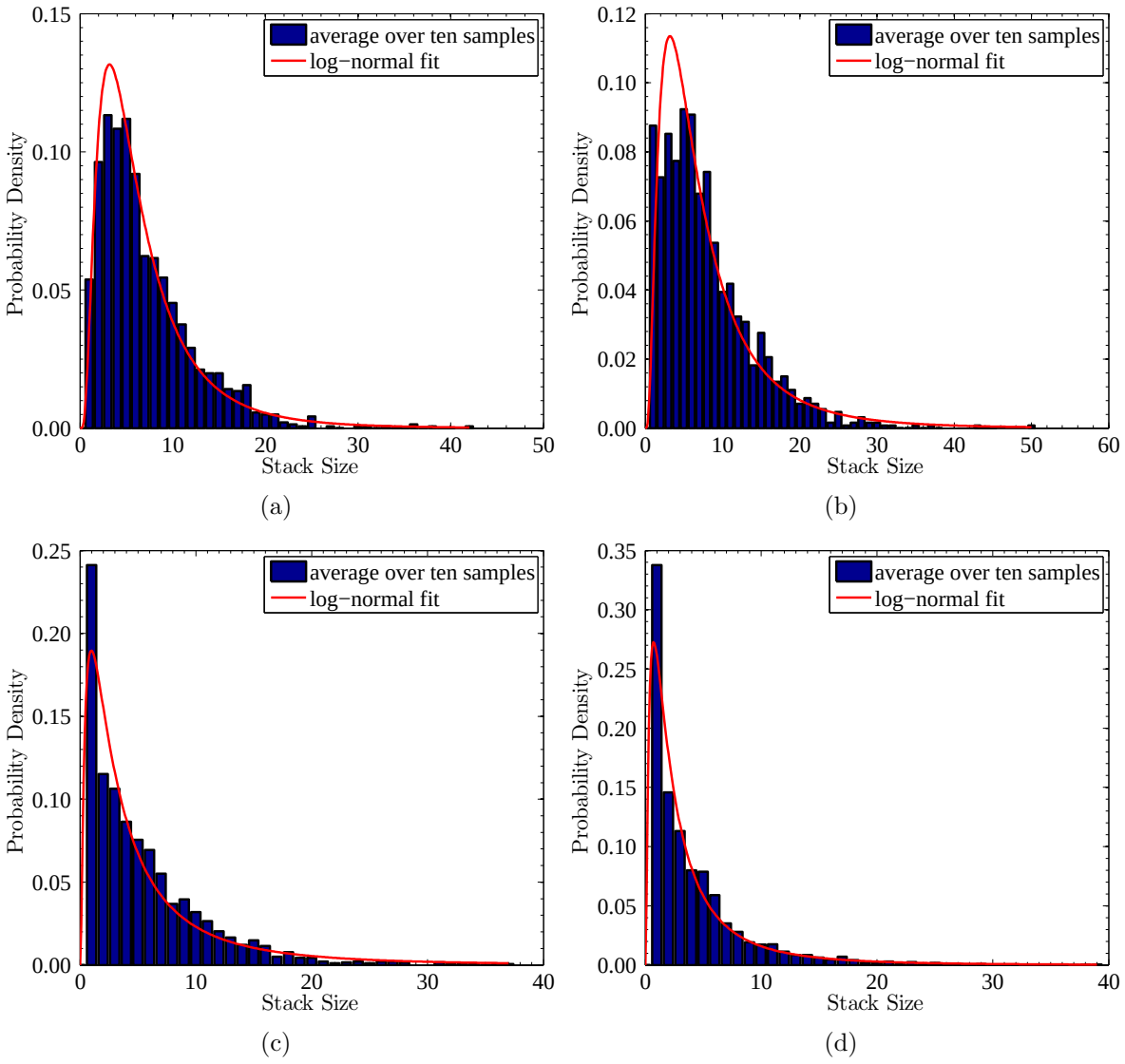

Figure 12: Probability distributions and fitted log-normal distributions to the stack size analysis for different types of simulations (P >1atm, see Table 3): (a) $1\dot{0}00$ Å (b) $1\dot{0}\dot{0}0$ Å (c) $1\dot{0}\ddot{0}0$ Å (d) $1\dot{0}\dddot{0}0$ Å

for $1\dot{0}00$ and $1\dot{0}\dot{0}0$, respectively). However, there is a more pronounced change in S for $1\dot{0}00/1\dot{0}\dot{0}0$ simulations vs $1\dot{0}0/5\dot{0}0$ cases (0.23/0.21 vs 0.10/0.11). In other words, as size of the platelets decreases the system becomes more isotropic since smaller particles have more freedom to move around due to their sizes. This is in agreement with experiments done by Hetzel et al.[69] who showed that lateral extension of particles decreases disorder in the geometrical arrangements of particles and the system becomes more anisotropic. Increasing

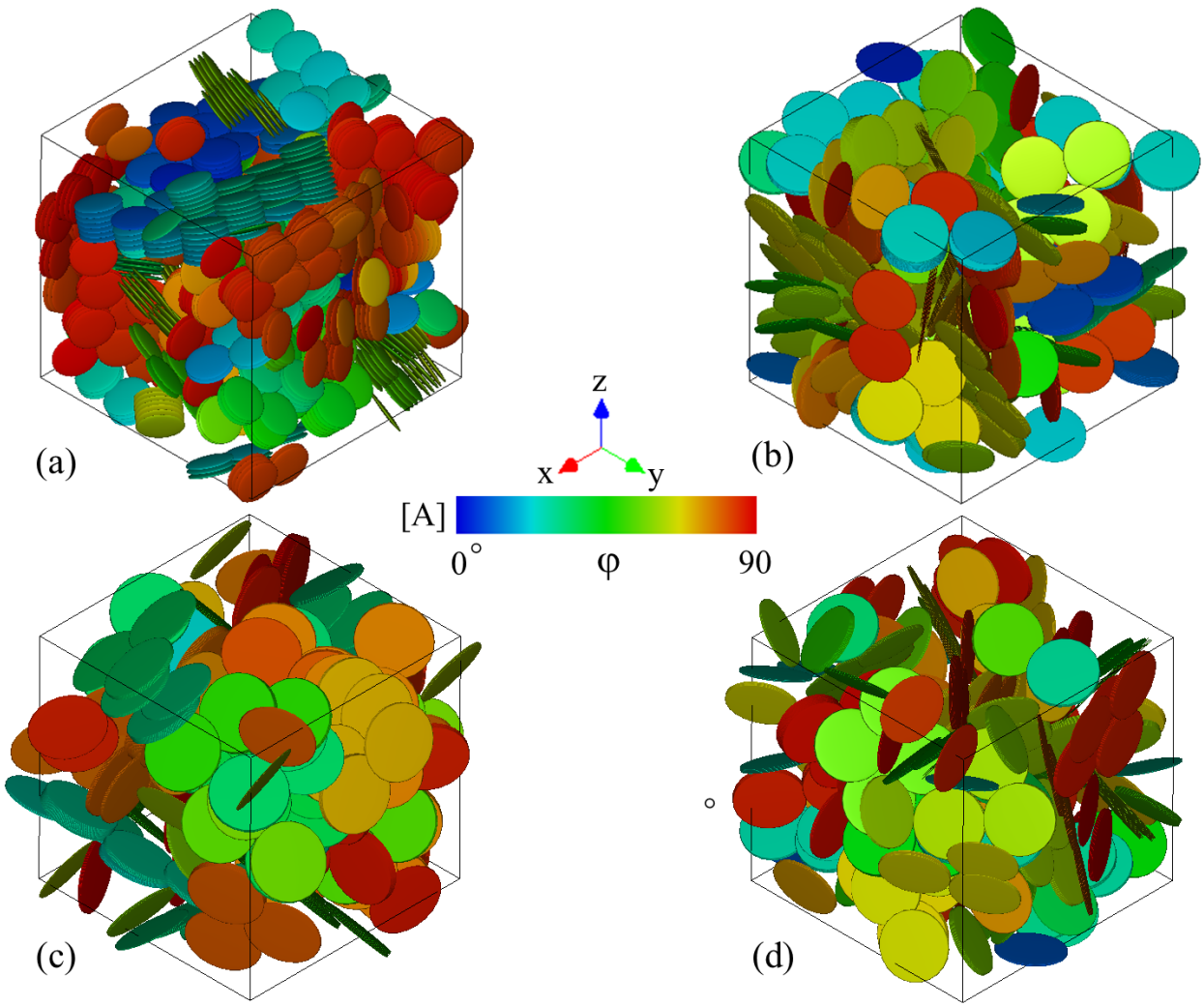

Figure 13: Equilibrated system from different types of simulations (P=1 atm, see Table 3): (a) $1\overset{\triangledown}{0}0$ Å (b) $5\overset{\triangledown}{0}0$ Å (c) $10\overset{\triangledown}{0}0$ Å (d) $10\overset{\triangledown\triangledown}{0}0$ Å. The particles orientations are color coded according to the ϕ angle, orientation of their normal vector with respect to the Z axis (colorbar A).

the confining pressure has a significant effect on ordering of particles reflected in an increase in the order parameter from S=0.23 to 0.46 for P=1 to 10 atm ($10\overset{\triangledown}{0}0$ vs $10\overset{\blacktriangledown}{0}0$ Table 4) then to 0.65 for P=50 atm (case $10\overset{\blacktriangledown\prime}{0}0$). More increase in pressure has small effect on the order parameter. The effect of pressure can be seen by comparing Figures 13(c) and 14. In summary, as pressure increases system becomes more ordered and the number of platelets per stack increases until reaching to the maximum ordered state (here at P=50 atm, case $10\overset{\blacktriangledown\prime}{0}0$, where we have S=0.65). More increase of the pressure decreases the average stack size

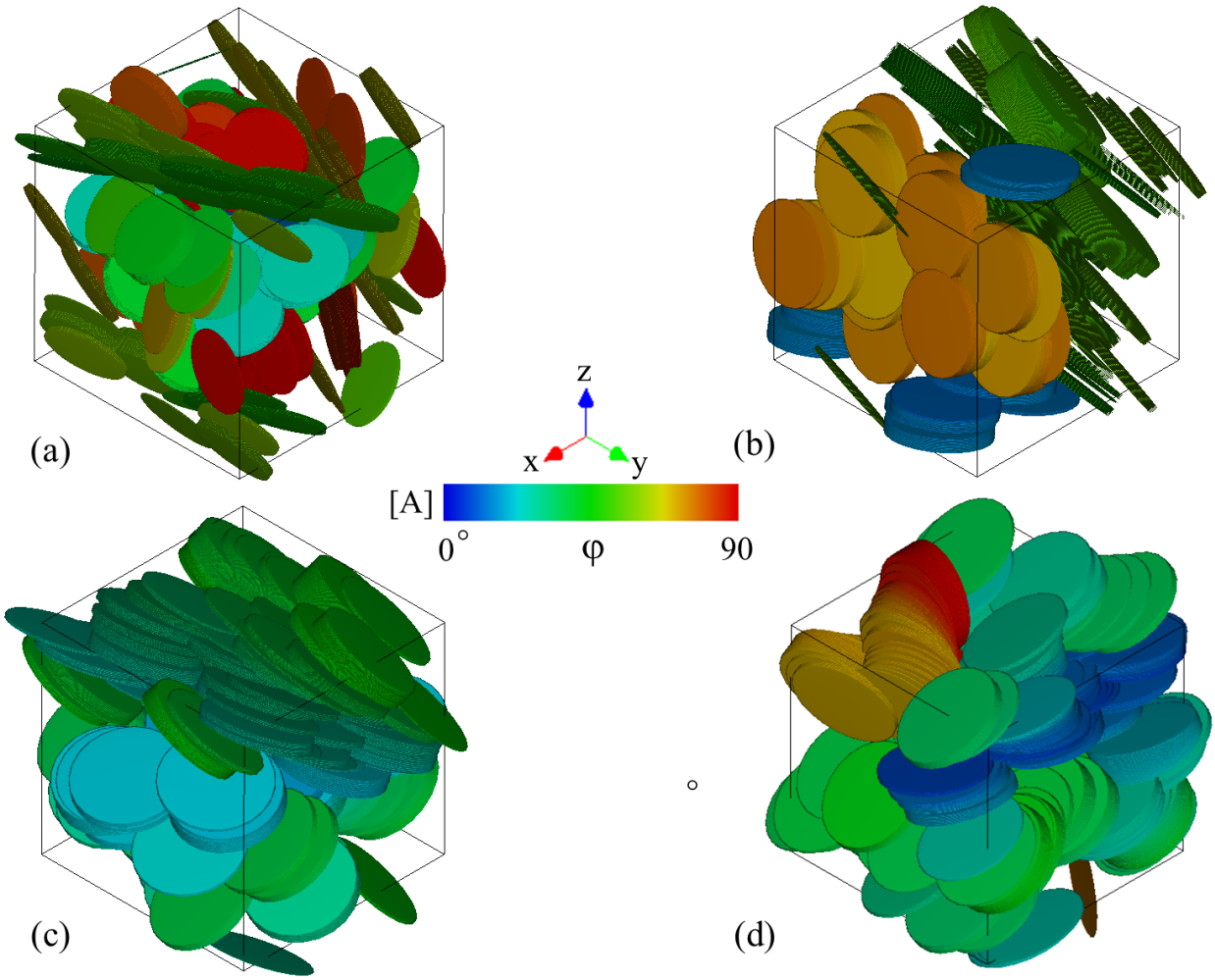

Figure 14: Equilibrated system from different types of simulations (P >1 atm, see Table 3): (a) $1\dot{0}00$ Å (b) $1\dot{0}'00$ Å (c) $1\dot{0}''00$ Å (d) $1\dot{0}'''00$ Å. The particles orientations are color coded according to the ϕ angle, orientation of their normal vector with respect to the Z axis (colorbar A).

due to sliding of platelets at fixed orientation (constant S). This result shows much smaller deviations in particle orientations at high confining pressure such that platelets can cross energy barriers, and as a result, become more aligned. Increasing pressure results in increasing concentration of particles due to decrease in volume. This result is in agreement with isotropic (orientationally disordered) to nematic (orientationally ordered) phase transition for nonspherical charged objects known as the Onsager transition.[70] According to Onsager theory at low concentration the system of particles is isotropic and orientational entropy of

particles are maximum. As the density of particles increases, nonspherical objects start to align to maximize the free volume in which they can move leading to the nematic phase.

Calculation of Elastic Properties of Meso-Scale Aggregate Assemblies

We have used quasi-static algorithm to construct stress-strain behaviors and interpret elastic stiffness properties of the particle assemblies with 500 Å and 1000 Å platelets. This algorithm consists of two steps: (1) application of a small homogeneous strain to the system (2) minimization of the potential energy of the system. The procedure was used previously to build stress-strain curves for gold crystal structure.[71] We applied six different strains on the system and computed stress components. The elastic constants are determined from Hooke's law:

$$\sigma_{ij} = \sum_{k,l} C_{ijkl}\epsilon_{kl} \tag{14}$$

Where C_{ijkl} represents fourth order elasticity tensor and ϵ_{kl} is the kl element of the second order strain tensor. We use the Voigt notation in representing components of the C_{ijkl} with indices: 11→1, 22→2, 33→3, 23→4, 13→5 and 12→6. In this notation, fourth order elasticity tensor can be represented by a symmetrical matrix with components C_{ij}. In the Cartesian coordinate indices 1,2 and 3 map to x, y and z, respectively. The internal stress tensor of the system are given by[72] :

$$\sigma_{ij} = \frac{1}{V}\sum_{\alpha}\left(m^{\alpha}v_i^{\alpha}v_j^{\alpha} + \sum_{\beta} f_i^{\alpha\beta}r_j^{\alpha\beta}\right) \tag{15}$$

Where V is the volume of the system, m^{α} and v^{α} are mass and velocity of platelet α, respectively. $f_i^{\alpha\beta}$ is the force acting on platelet α by platelet β in the i direction and $r_j^{\alpha\beta}$ is the Cartesian component of the vector from platelet β to platelet α in the j direction. Compressive and shear strain steps applied using an (NVT) ensemble (T=0.01 K). Each strain

Table 5: Details of simulations to calculate elastic properties. dt: time step, dϵ: strain step, n_s: number of steps, t_r and t_s: relaxation time and sampling period for each strain step. Symbols as in Table 2.

	GB calibration case	
	$\overset{\triangledown}{500}$	$\overset{\triangledown}{1000}$ & $\overset{\triangledown\triangledown}{1000}$ & $\overset{\blacktriangledown}{1000}$ & $\overset{\blacktriangledown\prime}{1000}$ & $\overset{\blacktriangledown\prime\prime}{1000}$& $\overset{\blacktriangledown\prime\prime\prime}{1000}$
dt(fs)	5	5
dϵ	2.5×10^{-5}	5×10^{-5}
n_s	25	50
t_r(ps)	800	100
t_s(ps)	80	10

step was relaxed over a relaxation time period. The stress values were averaged over the last ten percent of the relaxation time. Simulation details for calculation of elastic properties are summarized in Table 5. Elastic constants were obtained from a linear fit over the initial part of the stress strain curve representing values from ϵ =0 to 0.01% for 500 Å platelets and ϵ =0 to 0.03% for 1000 Å platelets. Figure 15 shows typical stress-strain curves used to calculate elasticity for a sample comprised of 500 Å platelets. Values of elastic properties

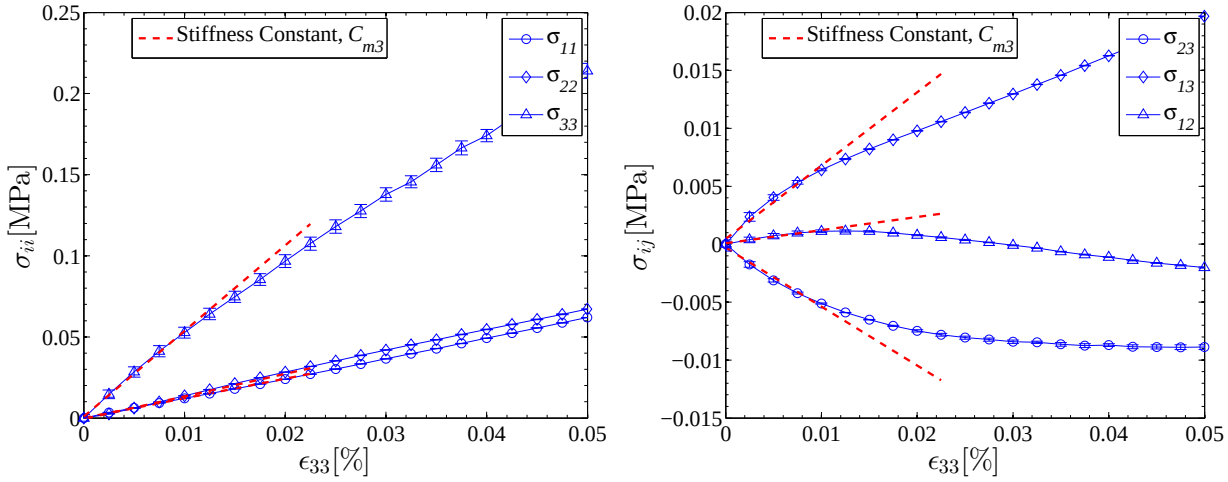

Figure 15: Stress-strain curves for a typical sample of 500 Å platelets. By applying strain in the z direction, ϵ_{33}, associated column in the stiffness matrix can be determined. (a) σ_{ii}-ϵ_{33} curves. m=1,2,3 (b) σ_{ij}-ϵ_{33} curves. m=4,5,6

are averaged over ten samples for each type of simulation (i.e., each GB calibration case).

Table 6 summarizes the mean and standard deviation of the elastic constants.

It can be seen that diagonal terms can be approximated with two parameters: $\overline{C}_{11} = 1/3\,(C_{11} + C_{22} + C_{33})$ and $\overline{C}_{44} = 1/3\,(C_{44} + C_{55} + C_{66})$. For instance, in the case of 500 Å the normal stiffness values are 0.51, 0.50 and 0.52 GPa ($\sim$ 0.51 GPa) and shear stiffness values are 0.1, 0.1 and 0.09 GPa ($\sim$ 0.1 GPa). In the off diagonal terms, C_{12}, C_{13} and C_{23} are close together and one order of magnitude larger than the rest of the off diagonal terms. For example, in the case of 500 Å the values of these terms are 0.12, 0.14 and 0.12 GPa ($\sim$ 0.13 GPa) , respectively, and the absolute values of the remaining off-diagonal terms are between 0.00-0.03 GPa. This suggests that the particle assemblies approximate cubic symmetry of the full elasticity tensor with three independent elastic constants: C_{11}, C_{12} and C_{44}. Table 7 summarizes the cubic average of the elastic properties calculated via simple averaging over the three directions, [100], [010] and [001]: $\overline{C}_{11}$, $\overline{C}_{44}$ and $\overline{C}_{12} = 1/3\,(C_{12} + C_{13} + C_{23})$. By increasing the size of the platelets, $\overline{C}_{11}$ increases from 0.51 GPa to 0.98 GPa. The increase in compressive stiffness is expected for larger platelets as the cohesion between the platelets increases due to the larger surface area. The value of $\overline{C}_{12}$ is related to the lateral Poisson's ratio connecting deformation between orthogonal axes. There is a negligible change in this elastic constant (from 0.13 to 0.14 GPa). Similarly the shear stiffness, $\overline{C}_{44}$, has a small change with changing size of the platelet (from 0.10 to 0.08 GPa). For a system equilibrated at larger pressures (cases $1\dot{0}00$, $1\dot{0}'00$, $1\dot{0}''00$ and $1\dot{0}'''00$), all elastic constants increase as expected. Comparing $1\dot{0}00$ and $1\dot{0}\dot{0}00$ cases shows decrease in all stiffness values for the case we have larger face-to-face distance at equilibrium condition. Shear stiffness decreases by 38% (from 0.08 to 0.05 GPa), normal stiffness decreases by 23% (from 0.98 to 0.75 GPa) and the stiffness related to Poisson's effect, $\overline{C}_{12}$, decreases by 21% (from 0.14 to 0.11 GPa). This change can be explained by difference in the width of the second energy well compared to the first (Figure 3(b)). As c<d the second derivative of the energy with respect to strain (i.e., elastic properties) are larger for GB calibrated to the first potential well.

The accuracy of the cubic-averaged elastic constants ($\overline{C}_{ij}$) in representing the full elastic

stiffness matrix was evaluated using Euclidean distance metric. This metric has been used previously to asses similarity between full elastic constant matrix and averaged symmetric one.[73] The Euclidean distance between two square matrices, $\mathbf{A_1}$ and $\mathbf{A_2}$, is calculated as follows:

$$d_E(\mathbf{A_1}, \mathbf{A_2}) = \|\mathbf{A_1} - \mathbf{A_2}\|_E \tag{16}$$

and the associated norm is defined by:

$$\|\mathbf{A}\|_E = \sqrt{tr\left(\mathbf{A}^T\mathbf{A}\right)} \tag{17}$$

where tr(·) stands for the trace and the superscript T denotes the transpose. Smaller values of the metric mean more similarity between matrices. Smaller values of this metric indicate better approximation of the full elastic matrix using cubic-averaged values. In other words, when there is no preferred direction in the microstructure, elastic constant values over three directions become close together and can be cubic-averaged to represent full elastic matrix. For each sample, the dimensionless Euclidean distance metric (divided by norm of the cubic averaged elastic matrix) was calculated. By averaging over ten samples, the mean and standard deviation of the metrics are reported in Table 7. By increasing platelet size, distance metric increases from 0.18 to 0.22. By applying confining pressure up to 10 atm we see a more pronounced increase to 0.43. Increasing pressure to 50 atm shows decrease in distance metric to 0.38 (case $\dot{1}\dot{0}\dot{0}\dot{0}'$) and metric starts to increase again as pressure increases (to 0.42 and 0.47 for P=300 atm and 800 atm, respectively). In general distance metric increases with pressure with an exception at P=50 atm. The exception occurs at the onset of the maximum ordering (S=0.65, case $\dot{1}\dot{0}\dot{0}\dot{0}'$). More increase of the pressure slides platelets against each other leading to more anisotropic system (compare Figures 14(a) and 14(b) with 14(c) and 14(d)). This is consistent with the change of microstructure. Figure 14 shows that there is less variation in particle orientation at higher pressure and hence, greater discrepancy from cubic symmetry approximation. Moreover a decrease in the order parameter S with decreas-

Table 6: Elastic constant properties (in GPa) calculated for 500 Å and 1000 Å platelets. Symbols as in Table 2.

	GB calibration case													
	$\overset{\triangledown}{500}$		$\overset{\triangledown}{1000}$		$\overset{\triangledown\triangledown}{1000}$		$\overset{\blacktriangledown}{1000}$		$\overset{\blacktriangledown\prime}{1000}$		$\overset{\blacktriangledown\prime\prime}{1000}$		$\overset{\blacktriangledown\prime\prime\prime}{1000}$	
	$< . >$	$\pm$	$< . >$	$\pm$	$< . >$	$\pm$	$< . >$	$\pm$	$< . >$	$\pm$	$< . >$	$\pm$	$< . >$	$\pm$
C_{11}	**0.51**	0.05	**0.96**	0.19	**0.76**	0.22	**3.58**	0.95	**5.69**	1.58	**12.89**	5.51	**26.00**	13.30
C_{22}	**0.50**	0.06	**1.07**	0.39	**0.74**	0.17	**4.02**	1.15	**7.42**	3.33	**15.37**	6.06	**33.47**	15.57
C_{33}	**0.52**	0.08	**0.92**	0.13	**0.75**	0.18	**4.59**	2.37	**6.15**	1.93	**14.24**	5.19	**28.02**	11.90
C_{44}	**0.10**	0.05	**0.09**	0.06	**0.05**	0.03	**0.42**	0.29	**0.75**	0.42	**2.06**	1.26	**5.22**	2.85
C_{55}	**0.10**	0.03	**0.07**	0.03	**0.06**	0.03	**0.46**	0.28	**0.54**	0.31	**1.53**	0.94	**4.20**	2.72
C_{66}	**0.09**	0.02	**0.09**	0.05	**0.05**	0.03	**0.43**	0.12	**0.70**	0.58	**2.13**	1.48	**4.62**	2.14
C_{12}	**0.12**	0.02	**0.14**	0.07	**0.11**	0.07	**0.49**	0.45	**1.36**	0.72	**4.24**	1.45	**8.60**	2.54
C_{13}	**0.14**	0.03	**0.13**	0.06	**0.11**	0.04	**0.57**	0.61	**0.97**	0.56	**3.75**	1.02	**8.46**	2.81
C_{14}	**−0.01**	0.02	**0.01**	0.03	**0.00**	0.02	**−0.02**	0.18	**−0.03**	0.25	**0.20**	0.47	**−0.49**	1.32
C_{15}	**0.00**	0.02	**0.04**	0.09	**0.00**	0.02	**0.18**	0.62	**0.43**	0.57	**−0.01**	1.73	**−0.18**	4.21
C_{16}	**0.00**	0.02	**0.03**	0.06	**0.01**	0.03	**−0.15**	0.61	**0.19**	0.32	**0.99**	1.07	**1.30**	1.99
C_{23}	**0.12**	0.03	**0.16**	0.09	**0.11**	0.04	**0.54**	0.42	**1.41**	0.60	**4.37**	1.49	**9.33**	2.97
C_{24}	**−0.03**	0.03	**0.02**	0.05	**0.02**	0.03	**0.33**	0.31	**0.20**	0.23	**0.00**	0.82	**0.18**	3.71
C_{25}	**−0.02**	0.02	**0.01**	0.05	**0.00**	0.02	**−0.03**	0.10	**0.05**	0.42	**−0.13**	1.08	**0.09**	2.78
C_{26}	**−0.01**	0.02	**0.01**	0.05	**0.03**	0.03	**0.14**	0.64	**0.26**	0.46	**0.81**	1.31	**1.53**	2.23
C_{34}	**−0.02**	0.03	**0.02**	0.07	**0.02**	0.02	**−0.15**	0.77	**0.02**	0.57	**0.29**	0.92	**−0.33**	4.45
C_{35}	**−0.02**	0.03	**0.01**	0.11	**0.01**	0.03	**0.11**	0.72	**0.05**	1.19	**−0.12**	1.83	**0.89**	5.18
C_{36}	**−0.01**	0.01	**0.02**	0.02	**0.01**	0.02	**0.00**	0.10	**0.26**	0.29	**0.39**	0.31	**0.54**	0.94
C_{45}	**0.01**	0.03	**0.00**	0.03	**0.01**	0.03	**0.00**	0.23	**0.11**	0.24	**0.26**	0.42	**0.30**	1.06
C_{46}	**0.00**	0.02	**−0.01**	0.08	**0.01**	0.03	**−0.01**	0.30	**0.26**	0.78	**−0.05**	0.43	**0.25**	0.78
C_{56}	**−0.01**	0.02	**−0.01**	0.03	**−0.01**	0.02	**−0.04**	0.12	**−0.12**	0.21	**0.00**	0.47	**−0.62**	1.51

ing platelet size (Table 4) indicates more randomness in orientation distribution for smaller platelets. This leads to better approximation of the elasticity matrix with cubic symmetry. Mechanical properties at the meso-scale should be validated against experimental data.

Nanoindentation is a submicrometer experiment used to measure material stiffness parameters. So far, we scaled up our simulations to submicron length scale, the scale accessible by indentation tests. We compared our meso-scale mechanical properties with the nanoindentation experiments performed by Bobko and Ulm[74] on different shale (highly compacted clay) samples. To compare our results, we calculated values of indentation modulus from

Table 7: Cubic averaged elastic properties (in GPa) and Euclidean distance between averaged and full elasticity tensors. Symbols as in Table 2.

	GB calibration case						
	$\overset{\triangledown}{500}$	$\overset{\triangledown}{1000}$	$\overset{\triangledown\triangledown}{1000}$	$\overset{\blacktriangledown}{1000}$	$\overset{\blacktriangledown\prime}{1000}$	$\overset{\blacktriangledown\prime\prime}{1000}$	$\overset{\blacktriangledown\prime\prime\prime}{1000}$
$\overline{C}_{11}$	0.51	0.98	0.75	4.07	6.42	14.17	29.16
$\overline{C}_{12}$	0.13	0.14	0.11	0.53	1.24	4.12	8.80
$\overline{C}_{44}$	0.10	0.08	0.05	0.44	0.66	1.91	4.68
$\frac{d_E(C_{ij},\overline{C}_{ij})}{\|\overline{C}_{ij}\|}$	0.18±0.05	0.22±0.08	0.17±0.07	0.43±0.11	0.38±0.12	0.42±0.12	0.47±0.10

elasticity components (C_{ij}) using the derivation by Delafargue and Ulm[75] for an orthotropic solid (see Appendix 1). Each value of packing density (one minus porosity) at the final state is calculated using 11 Å as the thickness of a platelet which corresponds to the minimum favorable face-to-face distance (Figure 3). Table 8 summarizes average packing density and indentation modulus for different types of simulations. In our upscaled model, values of indentation modulus show no preferrential direction (almost identical) which is consistent with cubic symmetry assumption for the elasticity tensor. The mean indentation modulus is used to compare with experiment. Figure 16 shows indentation modulus versus packing density from experiment and simulations. Three simulation points (associated with P=1 atm) lie on the left side of the graph (around packing density of 0.2) which correspond to colloidal clay system. The other indentation values from simulations of confined clay (P >1 atm) show a good agreement with simulation and the change follows the trend of the experiment.

Conclusions

Meso-scale aggregates of clay were studied using Gay-Berne potential calibrated from full atomistic simulations. The free energy of face-to-face and edge-to-edge interactions of clay platelets were calculated as the elementary configurations for calibration. Minima of the free energy are separated with $\sim$ 3 Å distance which corresponds to the diameter of a water

Table 8: Average packing density and indentation modulus (in GPa). Symbols as in Table 2.

	GB calibration case													
	$\overset{\triangledown}{500}$		$\overset{\triangledown}{1000}$		$\overset{\triangledown\triangledown}{1000}$		$\overset{\blacktriangledown}{1000}$		$\overset{\blacktriangledown'}{1000}$		$\overset{\blacktriangledown''}{1000}$		$\overset{\blacktriangledown'''}{1000}$	
	$<.>$	$\pm$	$<.>$	$\pm$	$<.>$	$\pm$	$<.>$	$\pm$	$<.>$	$\pm$	$<.>$	$\pm$	$<.>$	$\pm$
η	**0.23**	0.02	**0.21**	0.02	**0.20**	0.02	**0.43**	0.07	**0.63**	0.04	**0.77**	0.04	**0.87**	0.03
$\overline{M}_1$	**0.37**	0.03	**0.50**	0.11	**0.36**	0.15	**2.16**	0.61	**2.97**	0.83	**7.66**	3.02	**16.75**	7.32
$\overline{M}_2$	**0.36**	0.04	**0.55**	0.24	**0.35**	0.09	**2.22**	0.82	**3.82**	1.82	**8.99**	3.26	**20.50**	7.97
$\overline{M}_3$	**0.38**	0.07	**0.48**	0.13	**0.36**	0.10	**2.40**	1.29	**3.32**	1.15	**8.08**	2.41	**17.57**	6.28
$\overline{M}$	**0.37**	0.05	**0.51**	0.17	**0.36**	0.11	**2.26**	0.92	**3.37**	1.33	**8.24**	2.87	**18.27**	7.16

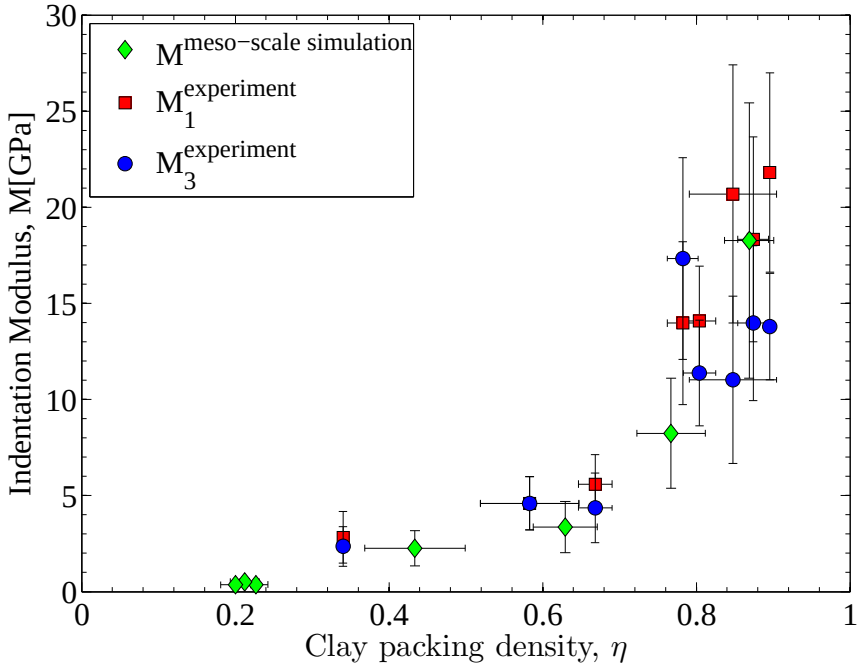

Figure 16: Indentation modulus versus clay packing density, η. The experimental data in the normal (x_3 direction) and parallel ($x_1(x_2)$ directions) to the bedding plane are taken from Bobko and Ulm[74].

molecule. The meso-scale simulations show that structural and mechanical properties of the aggregates are related to the clay platelet size and external applied pressure. Simulations for Wyoming Na-montmorillonite have shown that aggregate size distributions are well described by log-normal functions with mean stack size that increases from 3 to 8 platelets per aggregate. Smaller platelets have less order (more isotropic) structures while confining

pressure generates more ordered structures (more anisotropic).

The microstructure of the system of particles plays an important role in their mechanical properties. We found that larger aggregates produce more anisotropic structure with higher compressive and shear stiffness due to higher attraction between larger platelets. These features become more pronounced by increasing external pressure on the system until reaching to the maximum ordered state. More increase of the pressure, reduces aggregate size due to sliding of platelets against each other whereas mechanical properties are still increasing. While the size of the aggregates remains constant by their formation in the second energy minimum of face-to-face interaction, the mechanical properties of the microstructure decreases due to wider width of the second energy well.

Acknowledgments

The computational resources used for this project have been provided by the National Science Foundation through the Extreme Science and Engineering Discovery Environment (XSEDE) and the Texas Advanced Computing Center under grant TG-DMR100028. The first author wishes to acknowledge the X-Shale Hub at MIT and the Singapore-MIT Alliance for Research and Technology (SMART) for partial support of this project. The authors gratefully acknowledge Professor M. J. Buehler at MIT for useful discussions on the geometrical analysis of clay aggregates. We would also like to acknowledge advice and suggestion given by Professor G. C. Rutledge at MIT. We wish to thank M. J. Abdolhosseini Qomi and M. Pourmand for the fruitful discussions.

Appendix 1

The equations relating elastic constants (C_{ij}) to indentation modulus (M_1,M_2,M_3) for an orthotropic solid are summarized in this appendix[75]:

$$\begin{aligned} M_1 &\approx \sqrt{M_{12}M_{13}} \\ M_2 &\approx \sqrt{M_{21}M_{23}} \\ M_3 &\approx \sqrt{M_{31}M_{32}} \end{aligned} \tag{1.1}$$

where

$$\begin{aligned} M_{21} &= 2\sqrt{\frac{C_{11}C_{22}-C_{12}^2}{C_{11}}\left(\frac{1}{C_{66}}+\frac{2}{C_{11}C_{22}+C_{12}}\right)^{-1}} \\ M_{31} &= 2\sqrt{\frac{C_{11}C_{33}-C_{13}^2}{C_{11}}\left(\frac{1}{C_{55}}+\frac{2}{C_{11}C_{33}+C_{13}}\right)^{-1}} \\ M_{32} &= 2\sqrt{\frac{C_{22}C_{33}-C_{23}^2}{C_{22}}\left(\frac{1}{C_{44}}+\frac{2}{C_{22}C_{33}+C_{23}}\right)^{-1}} \end{aligned} \tag{1.2}$$

and

$$\begin{aligned} M_{12} &= M_{21}\sqrt{\frac{C_{11}}{C_{22}}} \\ M_{13} &= M_{31}\sqrt{\frac{C_{11}}{C_{33}}} \\ M_{23} &= M_{32}\sqrt{\frac{C_{22}}{C_{33}}} \end{aligned} \tag{1.3}$$

References

(1) Meunier, A. *Clay Minerals* **2006**, *41*, 551–566.

(2) Murray, H. H. *Applied clay science* **2000**, *17*, 207–221.

(3) Goldberg, S.; Glaubig, R. A. *Clays and Clay Minerals* **1987**, *35*, 220–7.

(4) Tombácz, E.; Csanaky, C.; Illés, E. *Colloid and Polymer Science* **2001**, *279*, 484–492.

(5) Lagaly, G.; Ziesmer, S. *Advances in Colloid and Interface Science* **2003**, *100*, 105–128.

(6) Tombácz, E.; Nyilas, T.; Libor, Z.; Csanaki, C. *From Colloids to Nanotechnology*; Springer, 2004; pp 206–215.

(7) Michot, L. J.; Bihannic, I.; Porsch, K.; Maddi, S.; Baravian, C.; Mougel, J.; Levitz, P. *Langmuir* **2004**, *20*, 10829–10837.

(8) Michot, L. J.; Bihannic, I.; Maddi, S.; Funari, S. S.; Baravian, C.; Levitz, P.; Davidson, P. *Proceedings of the National Academy of Sciences* **2006**, *103*, 16101–16104.

(9) García-García, S.; Wold, S.; Jonsson, M. *Journal of colloid and interface science* **2007**, *315*, 512–519.

(10) Michot, L. J.; Bihannic, I.; Maddi, S.; Baravian, C.; Levitz, P.; Davidson, P. *Langmuir* **2008**, *24*, 3127–3139.

(11) Zhou, D.; Abdel-Fattah, A. I.; Keller, A. A. *Environmental science & technology* **2012**, *46*, 7520–7526.

(12) Michot, L. J.; Bihannic, I.; Thomas, F.; Lartiges, B. S.; Waldvogel, Y.; Caillet, C.; Thieme, J.; Funari, S. S.; Levitz, P. *Langmuir* **2013**, *29*, 3500–3510.

(13) Carrier, B.; Wang, L.; Vandamme, M.; Pellenq, R. J.-M.; Bornert, M.; Tanguy, A.; Van Damme, H. *Langmuir* **2013**,

(14) Newman, A. *Chemistry of Clays and Clay Minerals*; Mineralogical Society monograph; Longman Scientific & Technical, 1987.

(15) Ebrahimi, D.; Pellenq, R. J.-M.; Whittle, A. J. *Langmuir* **2012**, *28*, 16855–16863.

(16) Dijkstra, M.; Hansen, J.; Madden, P. *Physical review letters* **1995**, *75*, 2236.

(17) Dijkstra, M.; Hansen, J.-P.; Madden, P. A. *Physical Review E* **1997**, *55*, 3044.

(18) Mourchid, A.; Delville, A.; Lambard, J.; Lecolier, E.; Levitz, P. *Langmuir* **1995**, *11*, 1942–1950.

(19) Kutter, S.; Hansen, J.-P.; Sprik, M.; Boek, E. *The Journal of Chemical Physics* **2000**, *112*, 311.

(20) Meyer, S.; Levitz, P.; Delville, A. *The Journal of Physical Chemistry B* **2001**, *105*, 9595–9602.

(21) Odriozola, G.; Romero-Bastida, M.; Guevara-Rodriguez, F. d. J. *Physical Review E* **2004**, *70*, 021405.

(22) Mossa, S.; De Michele, C.; Sciortino, F. *The Journal of chemical physics* **2007**, *126*, 014905.

(23) Jönsson, B.; Labbez, C.; Cabane, B. *Langmuir* **2008**, *24*, 11406–11413.

(24) Jardat, M.; Dufrêche, J.-F.; Marry, V.; Rotenberg, B.; Turq, P. *Physical Chemistry Chemical Physics* **2009**, *11*, 2023–2033.

(25) Thuresson, A.; Ullner, M.; Åkesson, T.; Labbez, C.; Jo?nsson, B. *Langmuir* **2013**, *29*, 9216–9223.

(26) Choudhury, N.; Pettitt, B. M. *Journal of the American Chemical Society* **2005**, *127*, 3556–3567.

(27) Gay, J.; Berne, B. *The Journal of Chemical Physics* **1981**, *74*, 3316.

(28) Chipot, C.; Pohorille, A. *Free energy calculations*; Springer, 2007.

(29) Cygan, R.; Liang, J.; Kalinichev, A. *The Journal of Physical Chemistry B* **2004**, *108*, 1255–1266.

(30) Liu, X.; Lu, X.; Wang, R.; Zhou, H.; Xu, S. *Clays and Clay Minerals* **2007**, *55*, 554.

(31) Suter, J.; Coveney, P.; Greenwell, H.; Thyveetil, M. *The Journal of Physical Chemistry C* **2007**, *111*, 8248–8259.

(32) Berendsen, H.; Grigera, J.; Straatsma, T. *Journal of Physical Chemistry* **1987**, *91*, 6269–6271.

(33) Van Der Spoel, D.; Lindahl, E.; Hess, B.; Groenhof, G.; Mark, A.; Berendsen, H.

Journal of computational chemistry **2005**, *26*, 1701.

(34) Humphrey, W.; Dalke, A.; Schulten, K. *Journal of molecular graphics* **1996**, *14*, 33–38.

(35) Refson, K.; Park, S.; Sposito, G. *The Journal of Physical Chemistry B* **2003**, *107*, 13376–13383.

(36) Nosé, S. *The Journal of chemical physics* **1984**, *81*, 511.

(37) Hoover, W. *Physical Review A* **1985**, *31*, 1695.

(38) Parrinello, M.; Rahman, A. *Journal of Applied Physics* **1981**, *52*, 7182–7190.

(39) Darden, T.; York, D.; Pedersen, L. *The Journal of Chemical Physics* **1993**, *98*, 10089.

(40) Essmann, U.; Perera, L.; Berkowitz, M.; Darden, T.; Lee, H.; Pedersen, L. *Journal of Chemical Physics* **1995**, *103*, 8577–8593.

(41) Ryckaert, J.-P.; Ciccotti, G.; Berendsen, H. J. *Journal of Computational Physics* **1977**, *23*, 327 – 341.

(42) Churakov, S. V. *The Journal of Physical Chemistry B* **2006**, *110*, 4135–4146.

(43) Churakov, S. V. *Geochimica et cosmochimica acta* **2007**, *71*, 1130–1144.

(44) Marry, V.; Rotenberg, B.; Turq, P. *Physical Chemistry Chemical Physics* **2008**, *10*, 4802–4813.

(45) Zwanzig, R. W. *The Journal of Chemical Physics* **1954**, *22*, 1420.

(46) Lee, C.; Scott, H. *The Journal of Chemical Physics* **1980**, *73*, 4591.

(47) Israelachvili, J. N.; Pashley, R. M. *Nature* **1983**, *306*, 249–250.

(48) Pashley, R. M.; Israelachvili, J. N. *Journal of colloid and interface science* **1984**, *101*, 511–523.

(49) Antognozzi, M.; Humphris, A.; Miles, M. *Applied Physics Letters* **2001**, *78*, 300–302.

(50) Fripiat, J.; Chaussidon, J.; Touillaux, R. *The Journal of Physical Chemistry* **1960**, *64*, 1234–1241.

(51) Russell, J.; Farmer, V. *Clay Minerals Bulletin* **1964**, *5*, 443–464.

(52) Malhotra, V.; Ogloza, A. *Physics and chemistry of minerals* **1989**, *16*, 386–393.

(53) Johnston, C.; Sposito, G.; Erickson, C. *Clays and Clay Minerals* **1992**, *40*, 722–730.

(54) Xu, W.; Johnston, C. T.; Parker, P.; Agnew, S. F. *Clays and Clay Minerals* **2000**, *48*, 120–131.

(55) Brown, W. M.; Petersen, M. K.; Plimpton, S. J.; Grest, G. S. *The Journal of chemical physics* **2009**, *130*, 044901.

(56) Plimpton, S. *Journal of Computational Physics* **1995**, *117*, 1–19.

(57) Brown, G.; Newman, A.; Rayner, J.; Weir, A. *The chemistry of soil constituents* **1978**, 29–178.

(58) Cadene, A.; Durand-Vidal, S.; Turq, P.; Brendle, J. *Journal of Colloid and Interface Science* **2005**, *285*, 719–730.

(59) Berardi, R.; Fava, C.; Zannoni, C. *Chemical physics letters* **1995**, *236*, 462–468.

(60) Everaers, R.; Ejtehadi, M. *Physical Review E* **2003**, *67*, 041710.

(61) Berardi, R.; Fava, C.; Zannoni, C. *Chemical physics letters* **1998**, *297*, 8–14.

(62) Gabriel, A. T.; Meyer, T.; Germano, G. *Journal of Chemical Theory and Computation* **2008**, *4*, 468–476.

(63) Chen, C.-T.; Ball, V.; de Almeida Gracio, J. J.; Singh, M. K.; Toniazzo, V.; Ruch, D.; Buehler, M. J. *ACS nano* **2013**, *7*, 1524–1532.

(64) Mystkowski, K.; Środoń, J.; Elsass, F. *Clay Minerals* **2000**, *35*, 545–557.

(65) Segad, M.; Jönsson, B.; Cabane, B. *The Journal of Physical Chemistry C* **2012**, *116*, 25425–25433.

(66) Tessier, D.; Pedro, G. Electron microscopy study of Na smectite fabricrole of layer charge, salt concentration and suction parameters. Proceedings of the International Clay Conference, Bologna and Pavia, Italy. 1981; pp 6–12.

(67) Pons, C.; Tessier, D.; Rhaiem, H. B.; Tchoubar, D.; Van Olphen, H.; Veniale, F. A comparison between X-ray studies and electron microscopy observations of smectite fabric. Proc. Int. Clay Conf., Bologna and Pavia. 1981; pp 177–185.

(68) Rhaiem, B. Factors affecting the microstructure of smectites–role of cation and history of applied stresses. Proceedings of the International Clay Conference. 1985; pp 292–7.

(69) Hetzel, F.; Tessier, D.; Jaunet, A.-M.; Doner, H. *Clays and clay minerals* **1994**, *42*, 242–242.

(70) Onsager, L. *Annals of the New York Academy of Sciences* **1949**, *51*, 627–659.

(71) Aghaei, A.; Abdolhosseini Qomi, M.; Kazemi, M.; Khoei, A. *International Journal of Solids and Structures* **2009**, *46*, 1925–1936.

(72) Vitek, V.; Egami, T. *physica status solidi (b)* **1987**, *144*, 145–156.

(73) Shahsavari, R.; Pellenq, R.; Ulm, F. *Phys. Chem. Chem. Phys.* **2010**, *13*, 1002–1011.

(74) Bobko, C.; Ulm, F.-J. *Mechanics of Materials* **2008**, *40*, 318–337.

(75) Delafargue, A.; Ulm, F.-J. *International journal of solids and structures* **2004**, *41*, 7351–7360.

Figure Captions

Figure 1 : (a) Part of the typical simulation setup for studying edge-to-edge interaction (red, O; white, H; yellow, Si; grey, Al; cyan, Mg; blue, Na). (b) Detail of the edge [0 1 0] structure. Si tetrahedra end with an SiO$\underline{\mathrm{H}}$ bond (top and bottom). Al octahedra end with AlOH inside the clay platelet and AlO$\underline{\mathrm{H}}_2$ on the broken edge. (c) Part of the typical simulation setup for studying face-to-face interaction.

Figure 2 : Potential of mean force for edge-to-edge interaction of clay platelets. (a) total PMF, a,b = 3.25, 3 Å , respectively. (b) PMF per length.

Figure 3 : Potential of mean force for face-to-face interaction of clay platelets. (a) total PMF, a,b = 3, 3.22 Å , respectively. (b) PMF per surface area. Width of the well is wider for the second minimum (d>c).

Figure 4 : Fitting parameters of the GB potential.

Figure 5 : Fitting GB potential to face-to-face and edge-to-edge interactions for different platelet diameters, D (a) D=$1\overset{\triangledown}{0}0$ Å (b) D=$5\overset{\triangledown}{0}0$ Å (c) D=$1\overset{\triangledown}{0}00$(or $1\overset{\blacktriangledown}{0}00$) Å, fitted to the first well of face-to-face interaction. (d) D=$1\overset{\triangledown\triangledown}{0}00$ Å, fitted to the second well of face-to-face interaction.

Figure 6 : Step function of applied pressure, p(t), in NPT simulations.

Figure 7 : Snapshots showing aggregation of one sample of $1\overset{\triangledown}{0}00$ Å platelets at: (a) t=40 ns (b) t=200 ns (c) t=1200 ns. The particles orientations are color coded according to the ϕ angle, orientation of their normal vector with respect to the Z axis (colorbar A).

Figure 8 : Total energy of the system of platelets for typical samples from simulations (see Table 3) (a) $1\overset{\triangledown}{0}00$ Å (b) $1\overset{\triangledown}{0}0$ Å .

Figure 9 : Percentage of kinetic energy to total energy in the last 200 ns of simulation for typical samples (see Table 3).

Figure 10 : Criteria used for analysis of aggregation. (a) distance criterion (b) orientation criterion.

Figure 11 : Probability distributions and fitted log-normal distributions to the stack size analysis for different types of simulations (P=1 atm, see Table 3): (a) $1\overset{\triangledown}{0}0$ Å (b) $5\overset{\triangledown}{0}0$ Å (c) $1\overset{\triangledown}{0}00$ Å (d) $1\overset{\triangledown\triangledown}{0}00$ Å

Figure 12 : Probability distributions and fitted log-normal distributions to the stack size analysis for different types of simulations (P >1atm, see Table 3): (a) $1\overset{\blacktriangledown}{0}00$ Å (b) $1\overset{\blacktriangledown\prime}{0}00$ Å (c) $1\overset{\blacktriangledown\prime\prime}{0}00$ Å (d) $1\overset{\blacktriangledown\prime\prime\prime}{0}00$ Å

Figure 13 : Equilibrated system from different types of simulations (P=1 atm, see Table 3): (a) $1\overset{\triangledown}{0}0$ Å (b) $5\overset{\triangledown}{0}0$ Å (c) $1\overset{\triangledown}{0}00$ Å (d) $1\overset{\triangledown\triangledown}{0}00$ Å. The particles orientations are color coded according to the ϕ angle, orientation of their normal vector with respect to the Z axis (colorbar A).

Figure 14 : Equilibrated system from different types of simulations (P >1 atm, see Table 3): (a) $1\overset{\blacktriangledown}{0}00$ Å (b) $1\overset{\blacktriangledown\prime}{0}00$ Å (c) $1\overset{\blacktriangledown\prime\prime}{0}00$ Å (d) $1\overset{\blacktriangledown\prime\prime\prime}{0}00$ Å. The particles orientations are color coded according to the ϕ angle, orientation of their normal vector with respect to the Z axis (colorbar A).

Figure 15 : Stress-strain curves for a typical sample of 500 Å platelets. By applying strain in the z direction, ϵ_{33}, associated column in the stiffness matrix can be determined. (a) σ_{ii}-ϵ_{33} curves. m=1,2,3 (b) σ_{ij}-ϵ_{33} curves. m=4,5,6

Figure 16 : Indentation modulus versus clay packing density, η. The experimental data in the normal (x_3 direction) and parallel ($x_1(x_2)$ directions) to the bedding plane are taken from Bobko and Ulm[74].

Figure 1

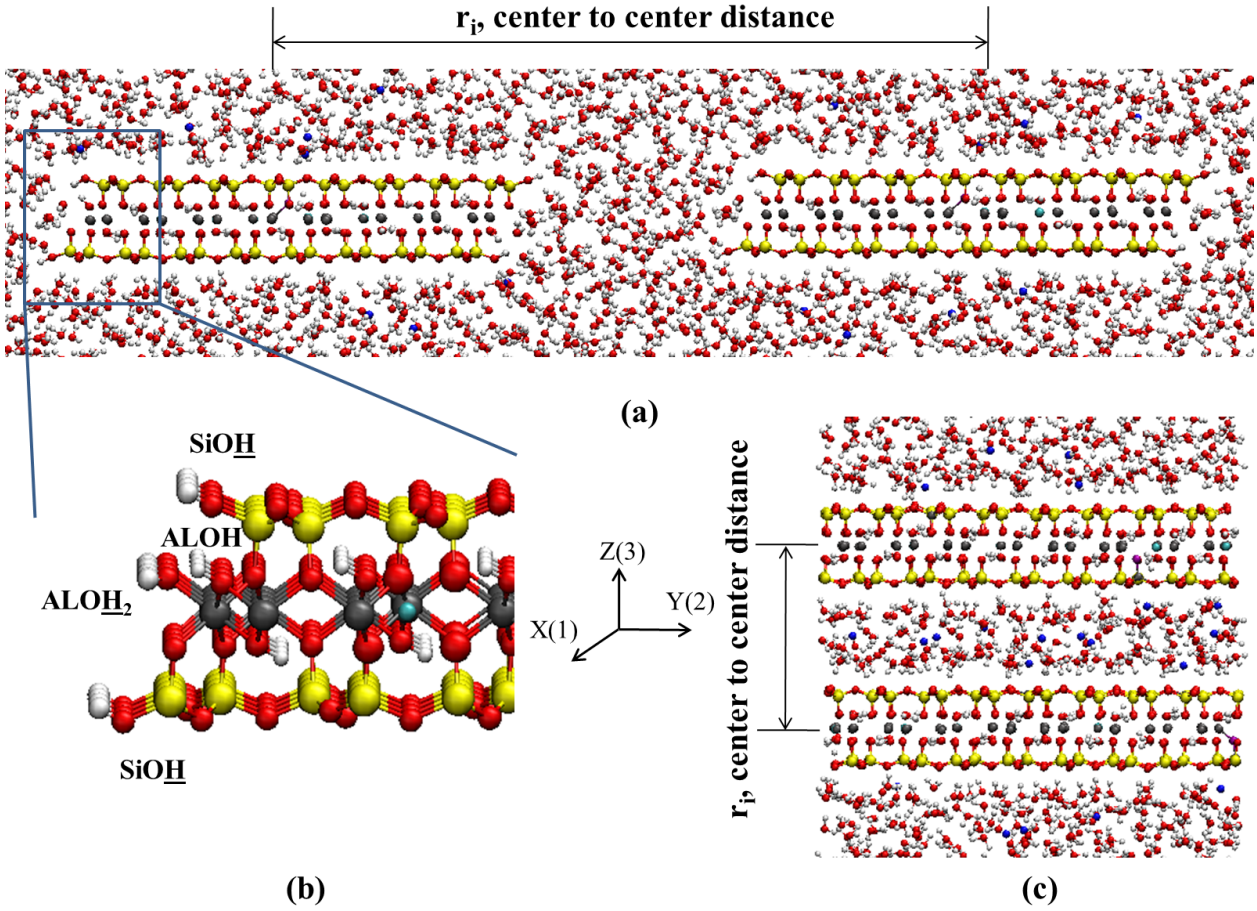
r_i, center to center distance
(a)
SiOH
ALOH
ALOH2
SiOH
Z(3)
Y(2)
X(1)
r_i, center to center distance
(b)
(c)

Figure 2

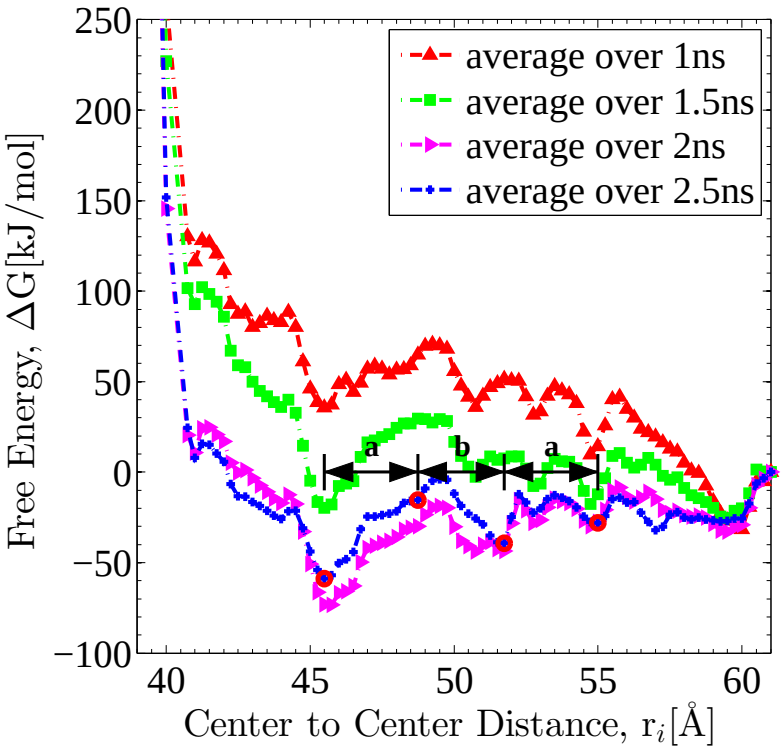
average over 1ns
average over 1.5ns
average over 2ns
average over 2.5ns
a
b
a
Free Energy, ΔG[kJ/mol]
Center to Center Distance, r$_i$[Å]
250
200
150
100
50
0
−50
−100
40
45
50
55
60

(a)

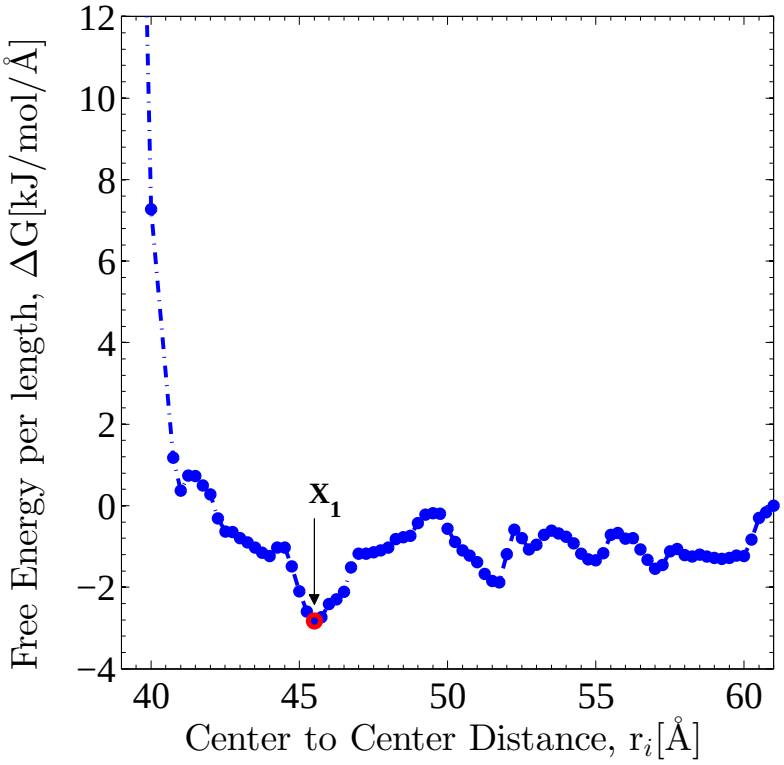
X$_1$
Free Energy per length, ΔG[kJ/mol/Å]
Center to Center Distance, r$_i$[Å]
12
10
8
6
4
2
0
−2
−4
40
45
50
55
60

(b)

Figure 3

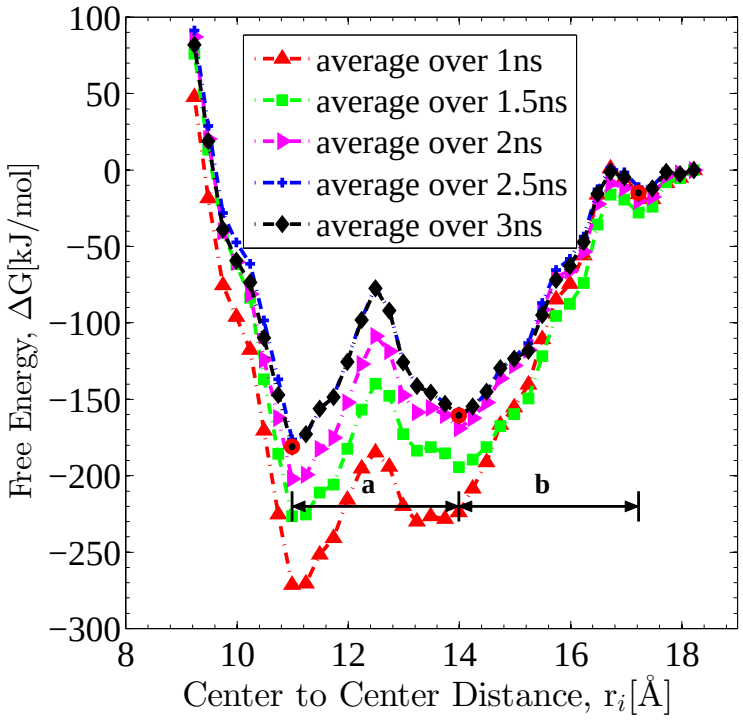
average over 1ns
average over 1.5ns
average over 2ns
average over 2.5ns
average over 3ns
a
b
Free Energy, ΔG[kJ/mol]
Center to Center Distance, r$_i$[Å]

(a)

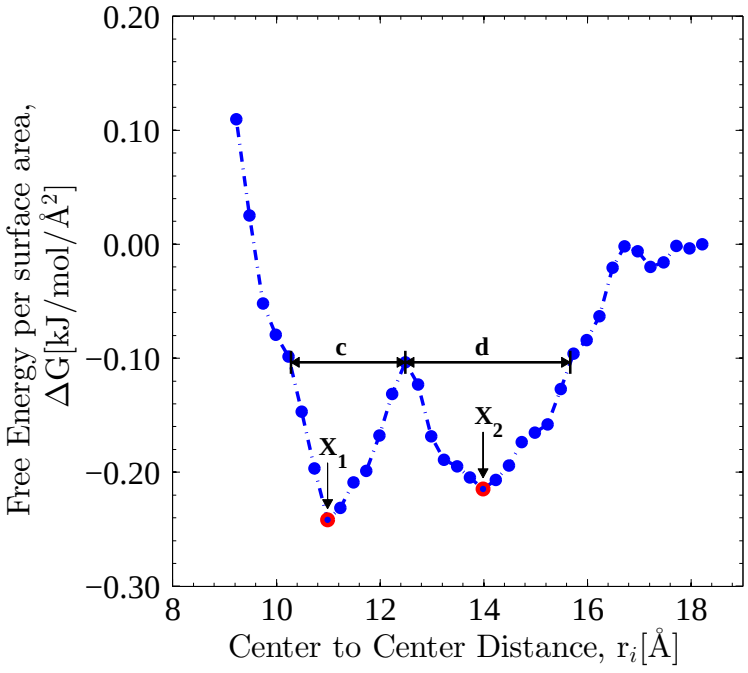
c
d
X$_1$
X$_2$
Free Energy per surface area, ΔG[kJ/mol/Å^2]
Center to Center Distance, r$_i$[Å]

(b)

Figure 4

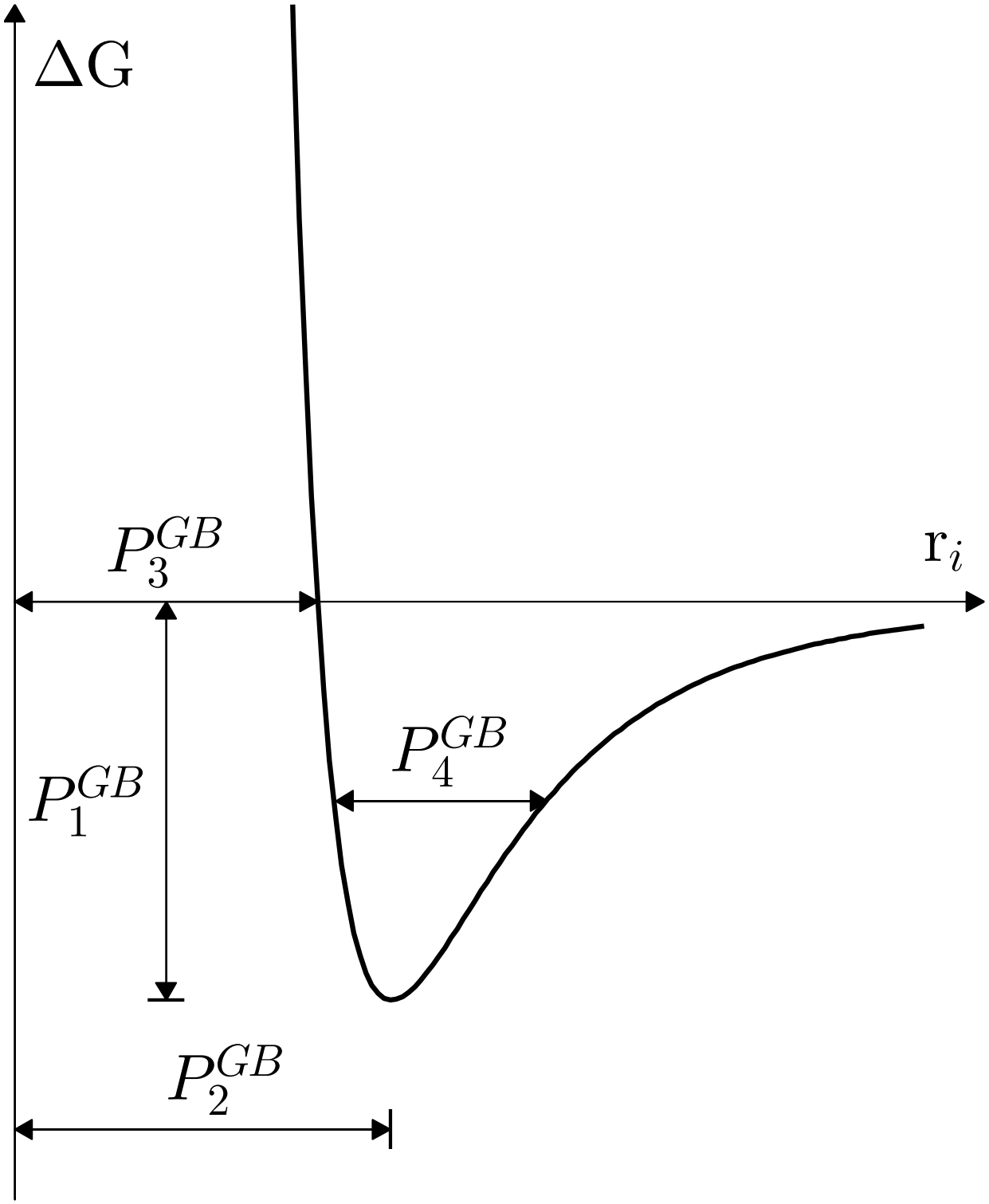

Figure 5

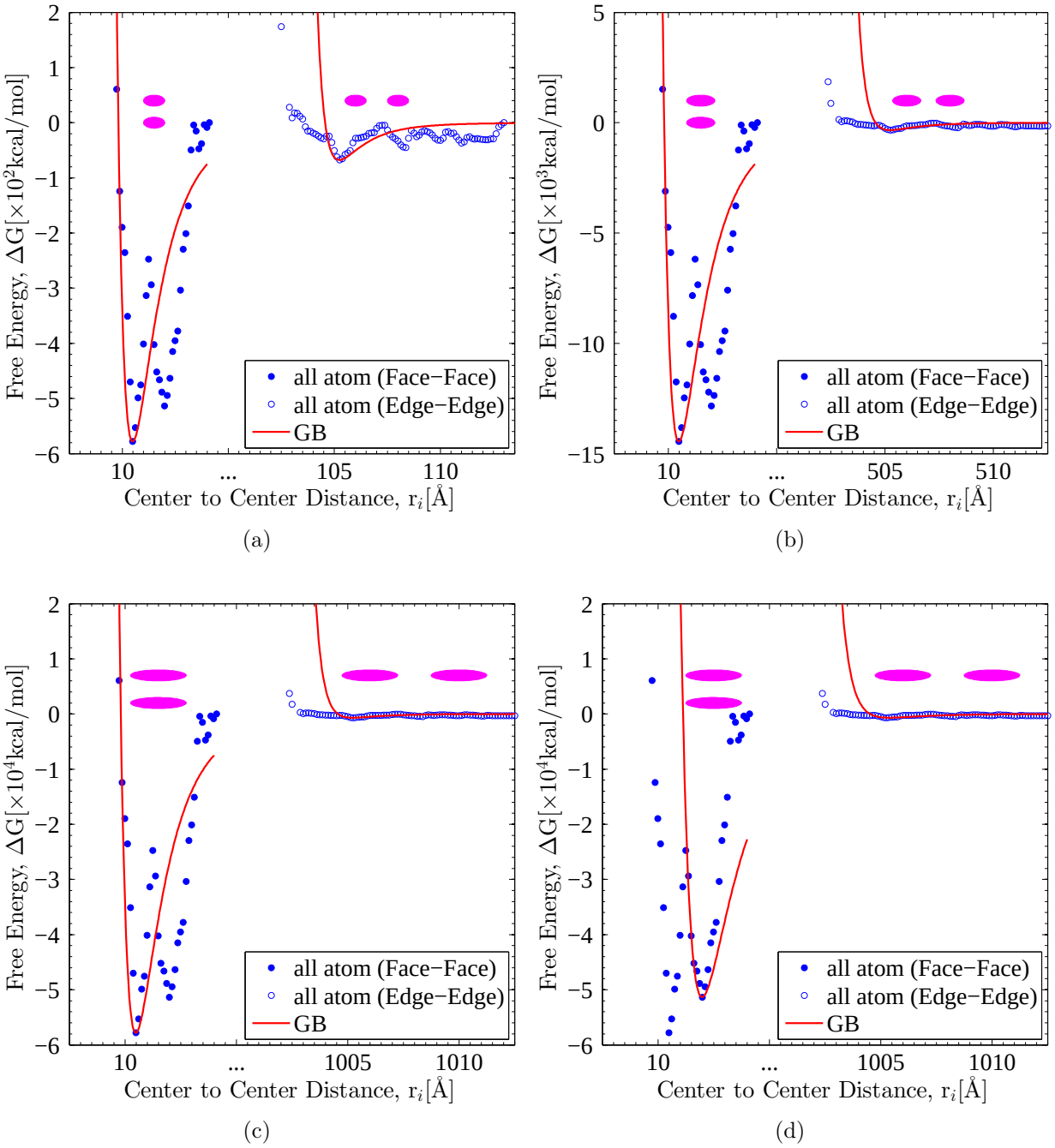
Free Energy, ΔG[×10^2kcal/mol]
Center to Center Distance, r_i[Å]
all atom (Face−Face)
all atom (Edge−Edge)
GB
(a)
Free Energy, ΔG[×10^3kcal/mol]
Center to Center Distance, r_i[Å]
all atom (Face−Face)
all atom (Edge−Edge)
GB
(b)
Free Energy, ΔG[×10^4kcal/mol]
Center to Center Distance, r_i[Å]
all atom (Face−Face)
all atom (Edge−Edge)
GB
(c)
Free Energy, ΔG[×10^4kcal/mol]
Center to Center Distance, r_i[Å]
all atom (Face−Face)
all atom (Edge−Edge)
GB
(d)

Figure 6

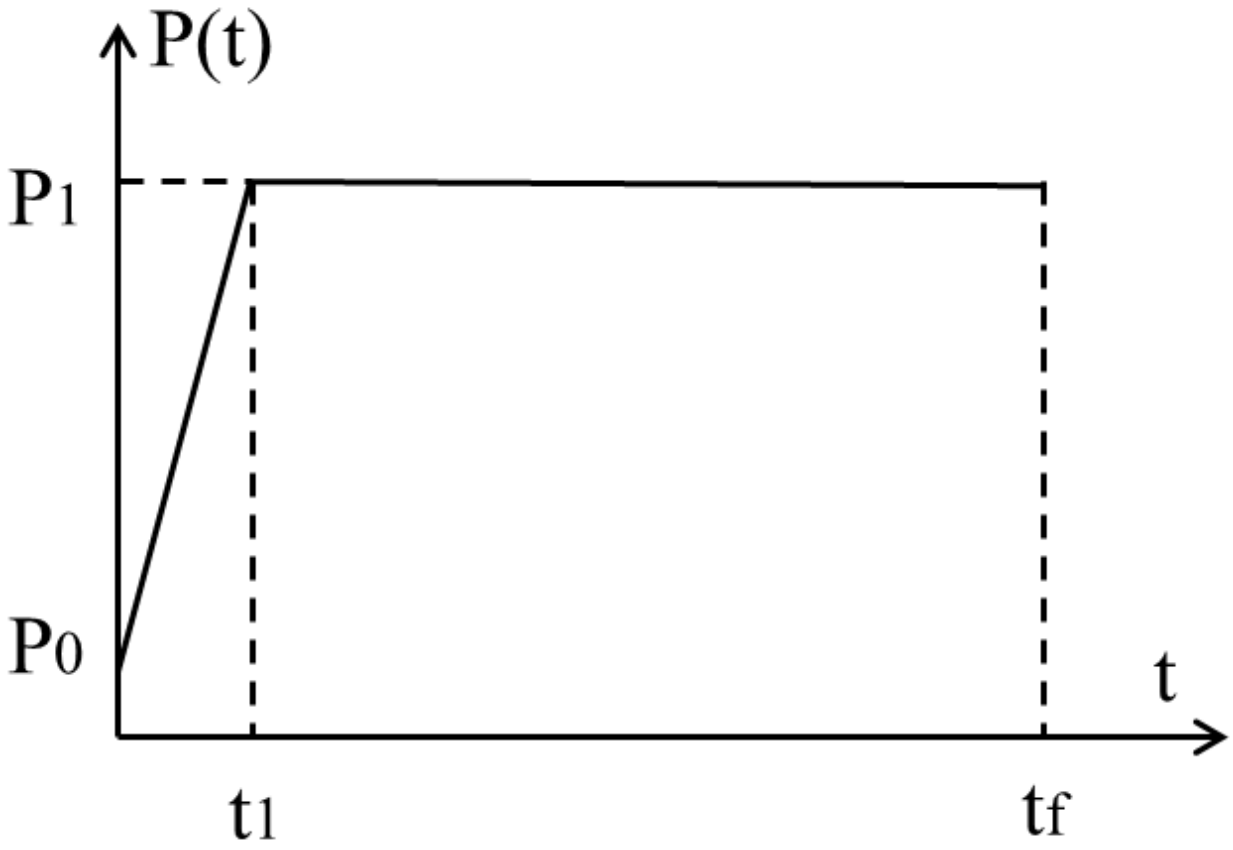

Figure 7

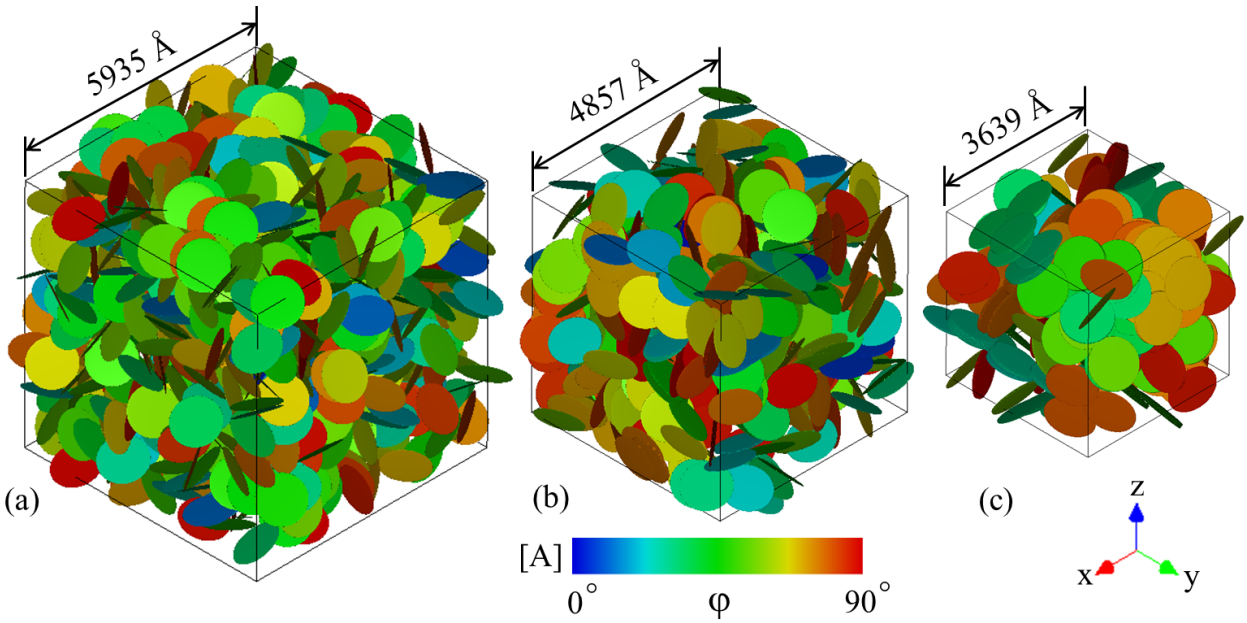

Figure 8

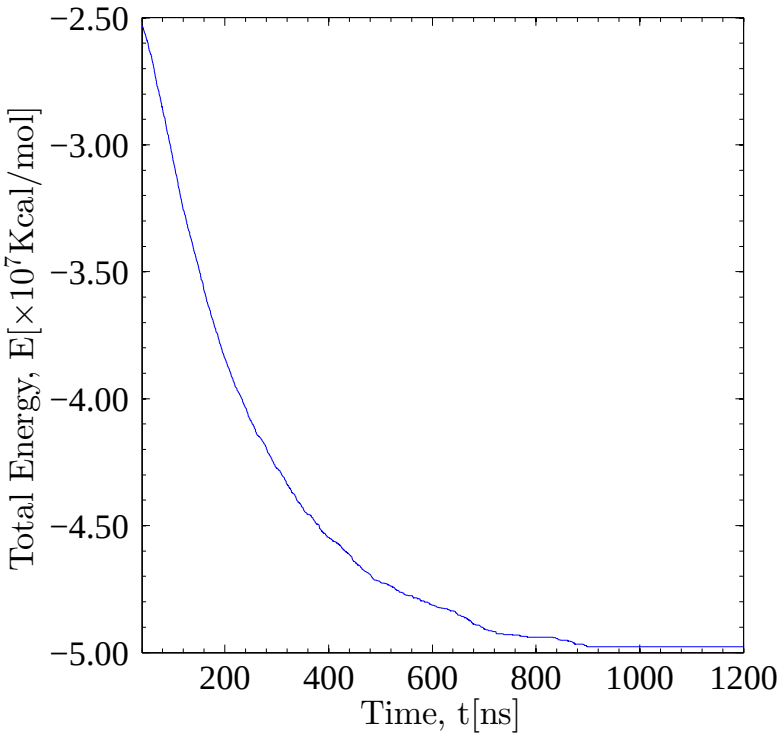
−2.50
−3.00
−3.50
−4.00
−4.50
−5.00
Total Energy, E[×10^7Kcal/mol]
200
400
600
800
1000
1200
Time, t[ns]

(a)

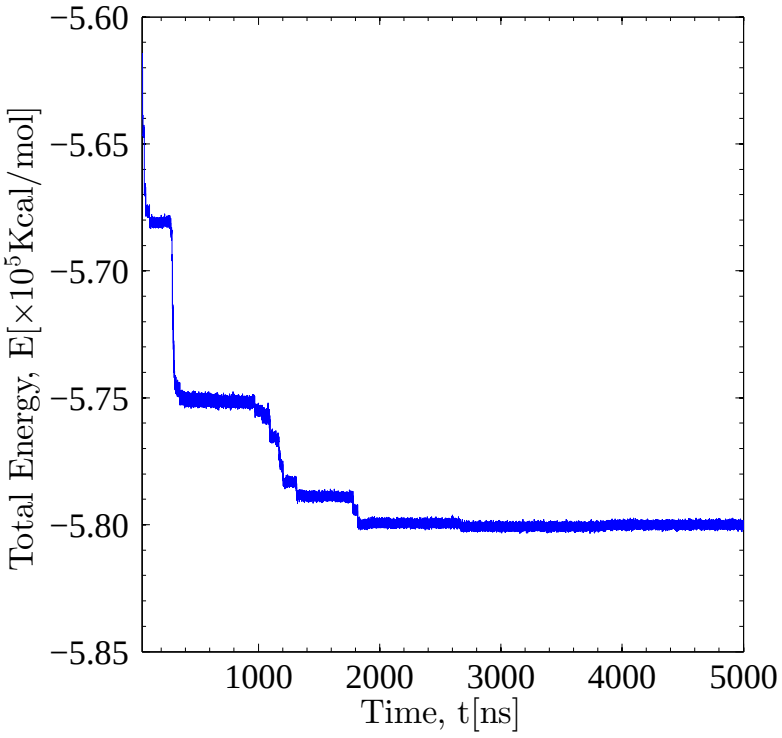
−5.60
−5.65
−5.70
−5.75
−5.80
−5.85
Total Energy, E[×10^5Kcal/mol]
1000
2000
3000
4000
5000
Time, t[ns]

(b)

Figure 9

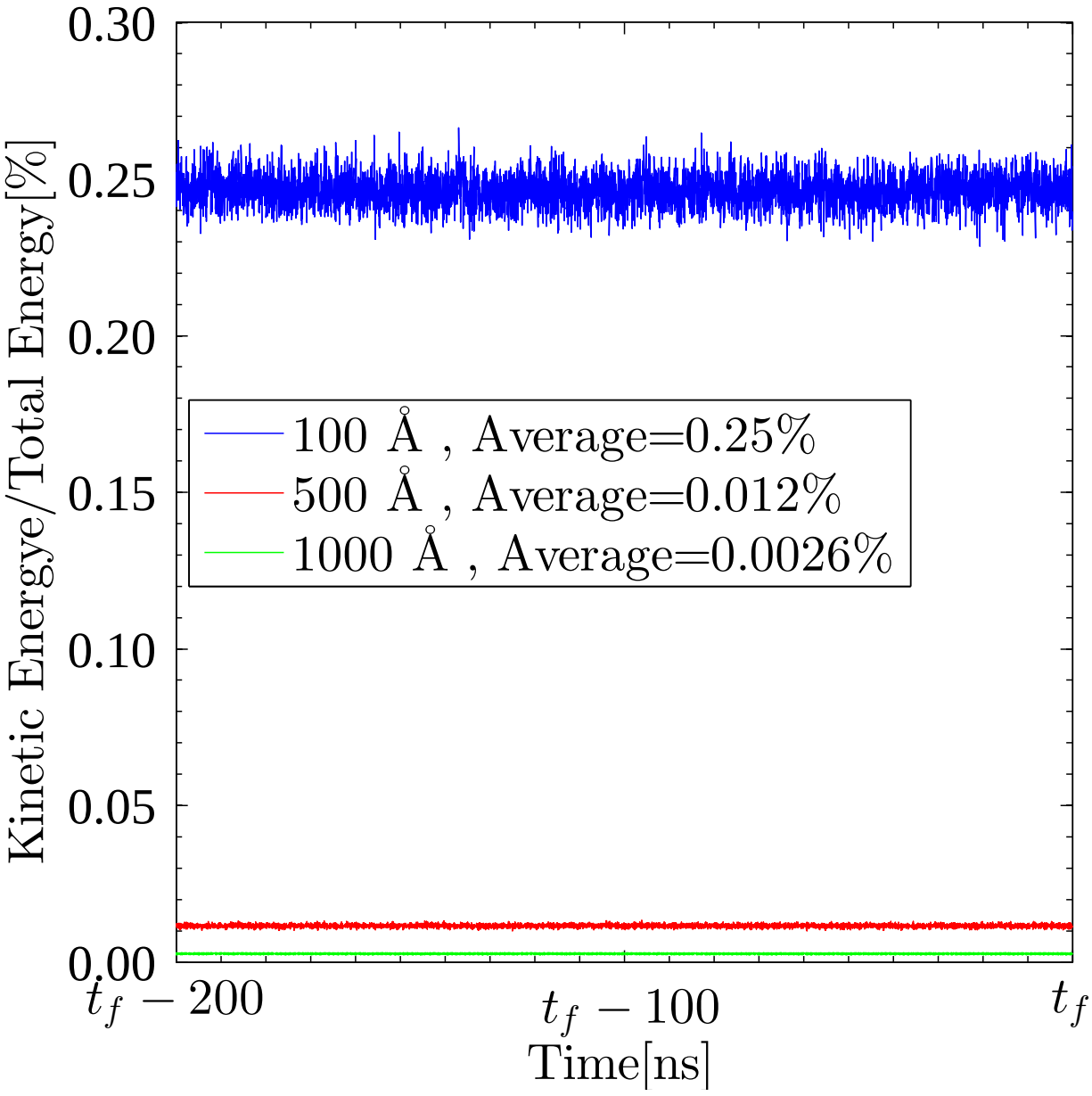
0.30
0.25
0.20
0.15
0.10
0.05
0.00
Kinetic Energye/Total Energy[%]
100 Å , Average=0.25%
500 Å , Average=0.012%
1000 Å , Average=0.0026%
$t_f - 200$
$t_f - 100$
t_f
Time[ns]

Figure 10

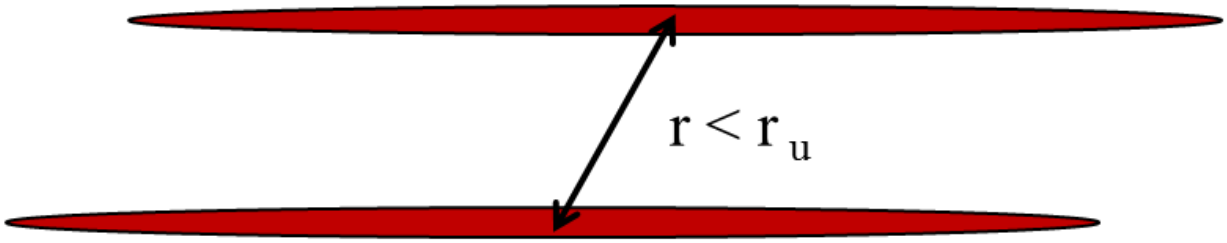

(a)

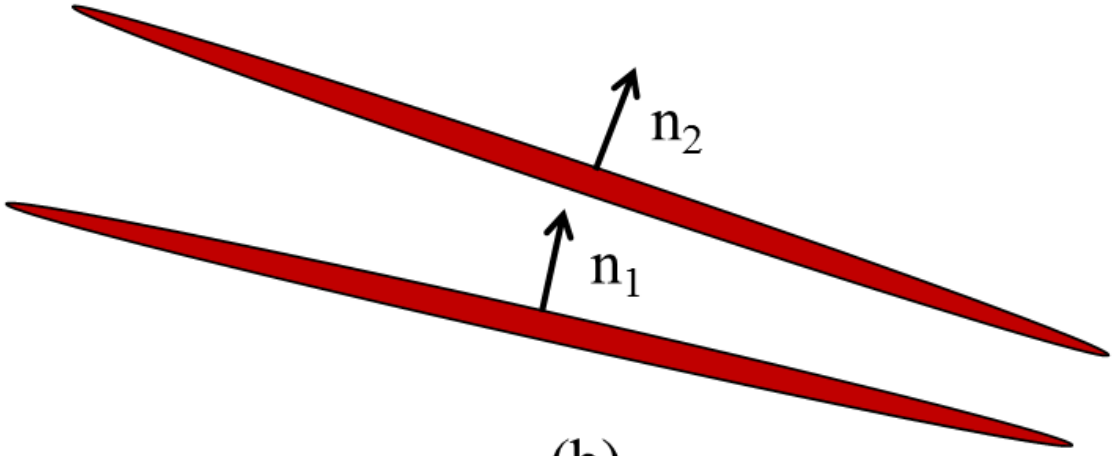

(b)

Figure 11

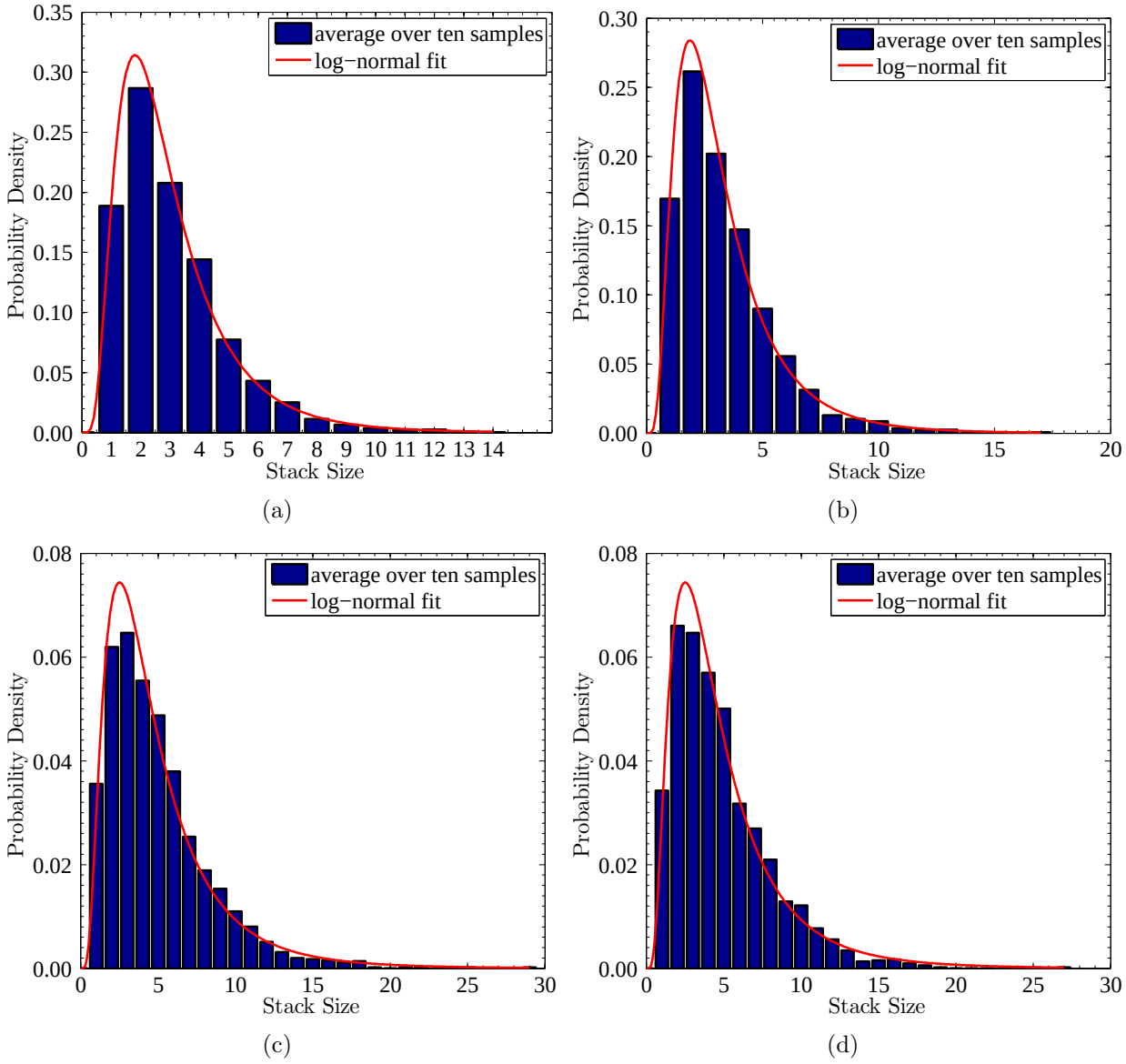
average over ten samples
log−normal fit
Probability Density
Stack Size
(a)
(b)
(c)
(d)

Figure 12

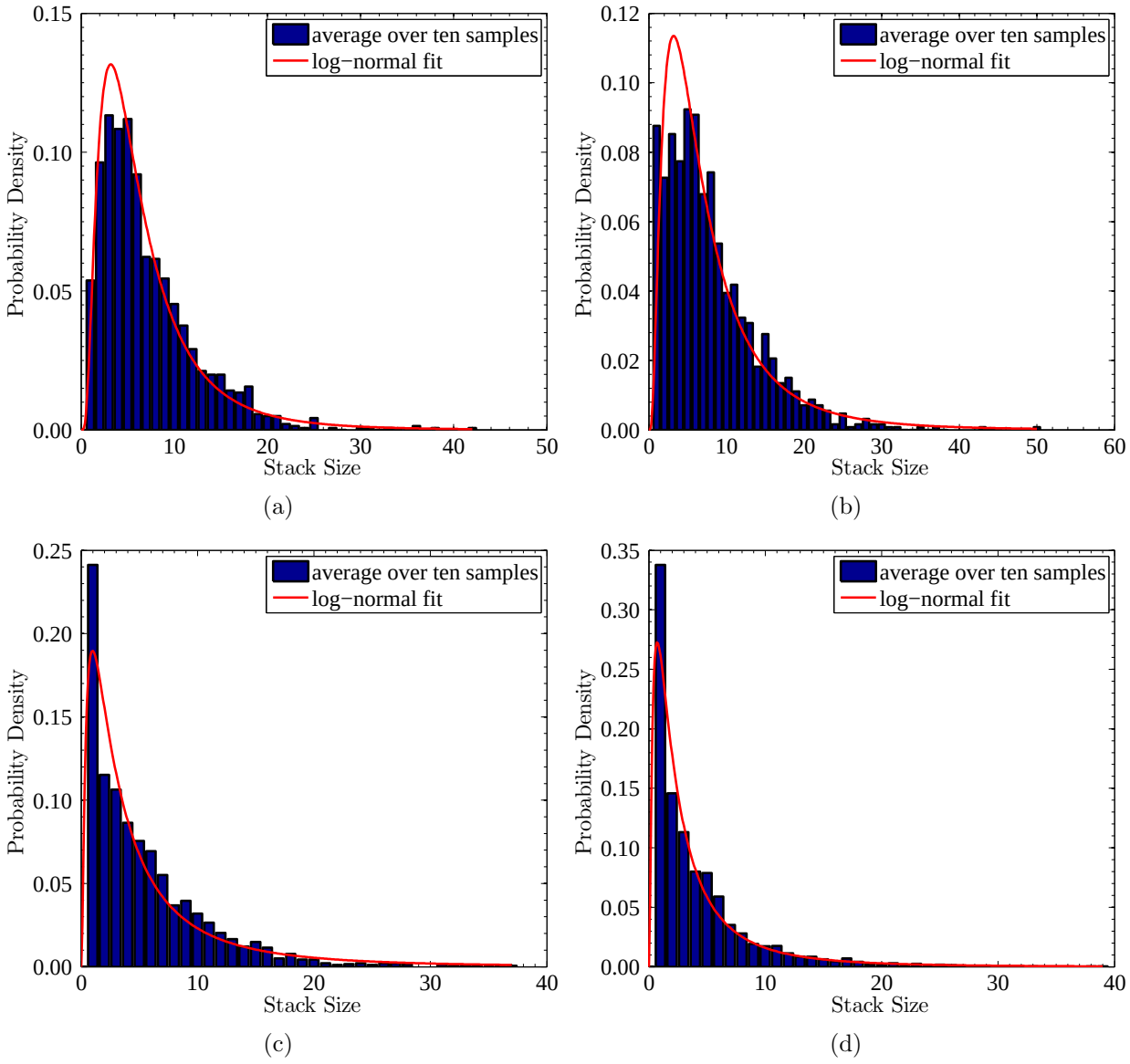
average over ten samples
log−normal fit
Probability Density
Stack Size
(a)
(b)
(c)
(d)

Figure 13

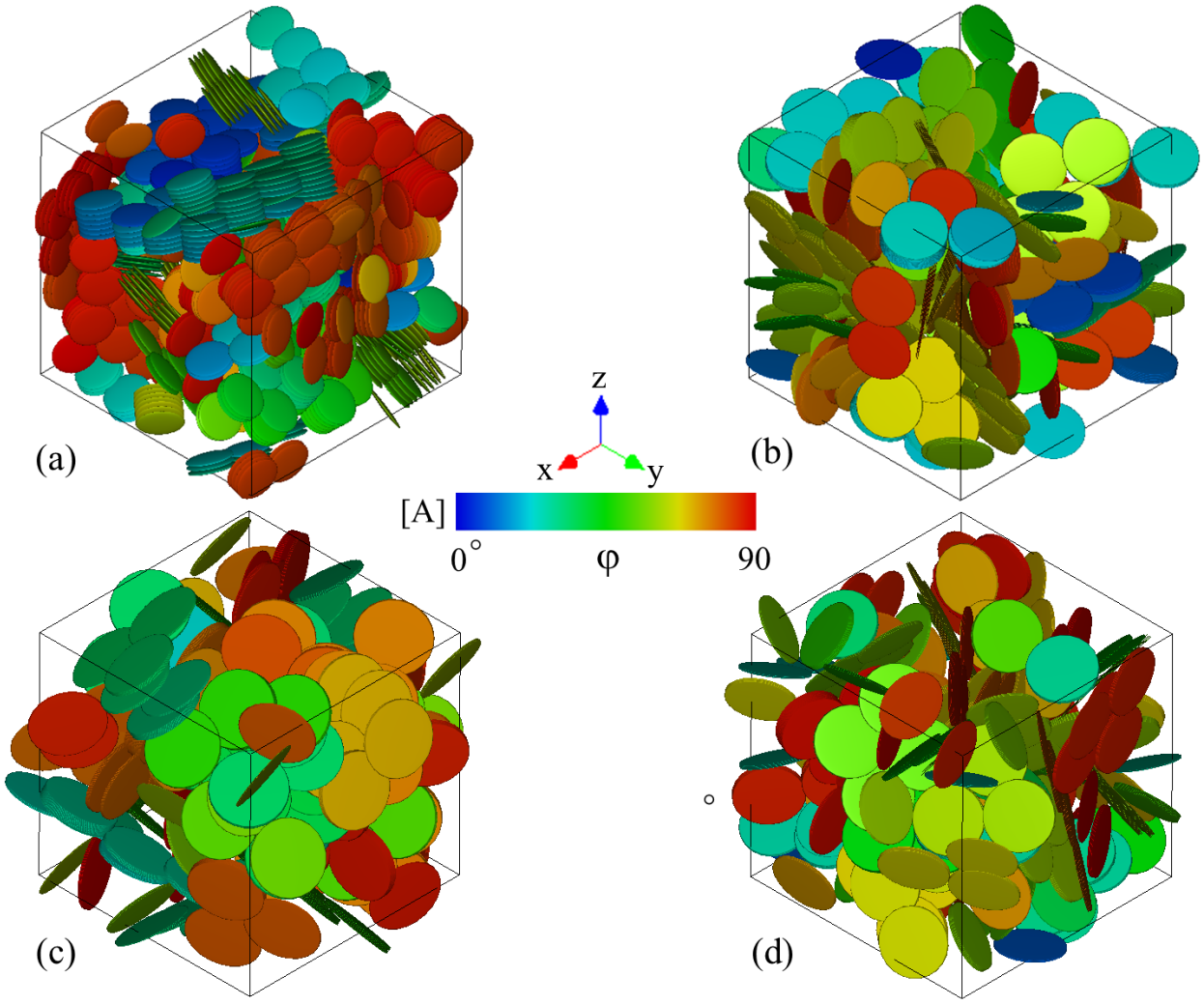

Figure 14

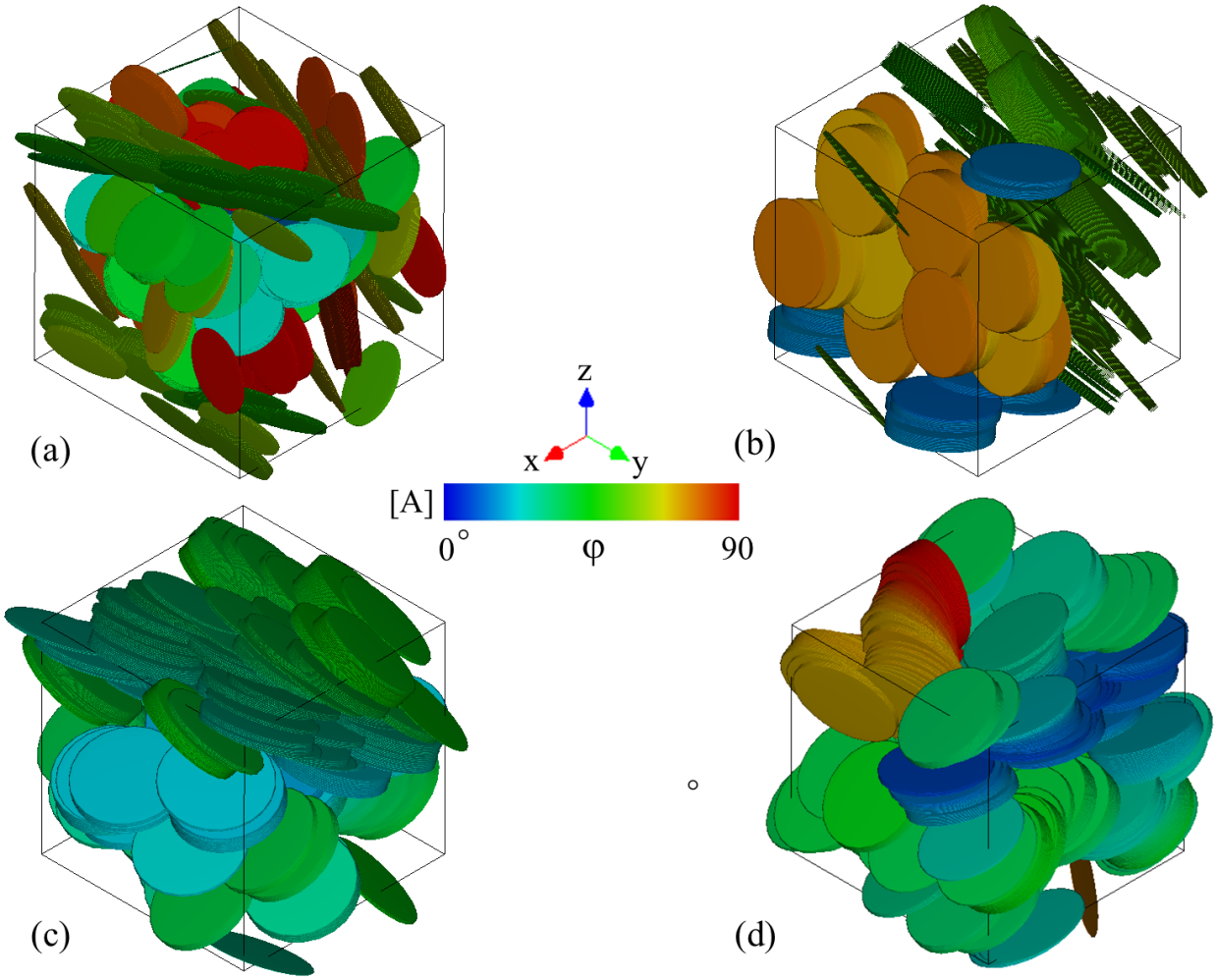

Figure 15

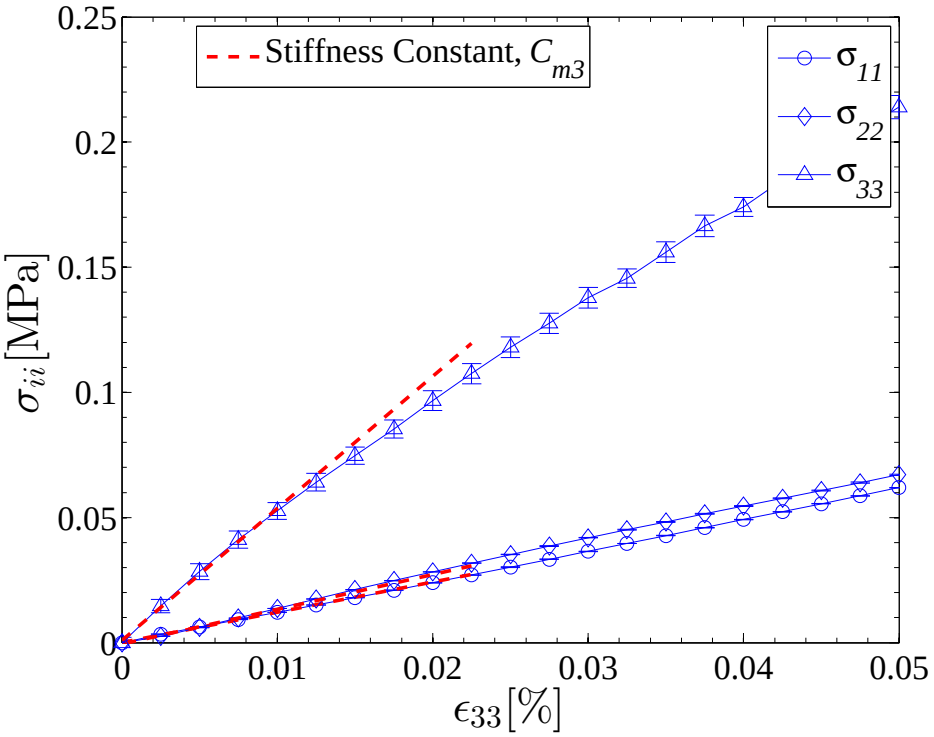
Stiffness Constant, C_{m3}
σ_{11}
σ_{22}
σ_{33}
σ_{ii} [MPa]
ϵ_{33} [%]
0.25
0.2
0.15
0.1
0.05
0
0.01
0.02
0.03
0.04
0.05

(a)

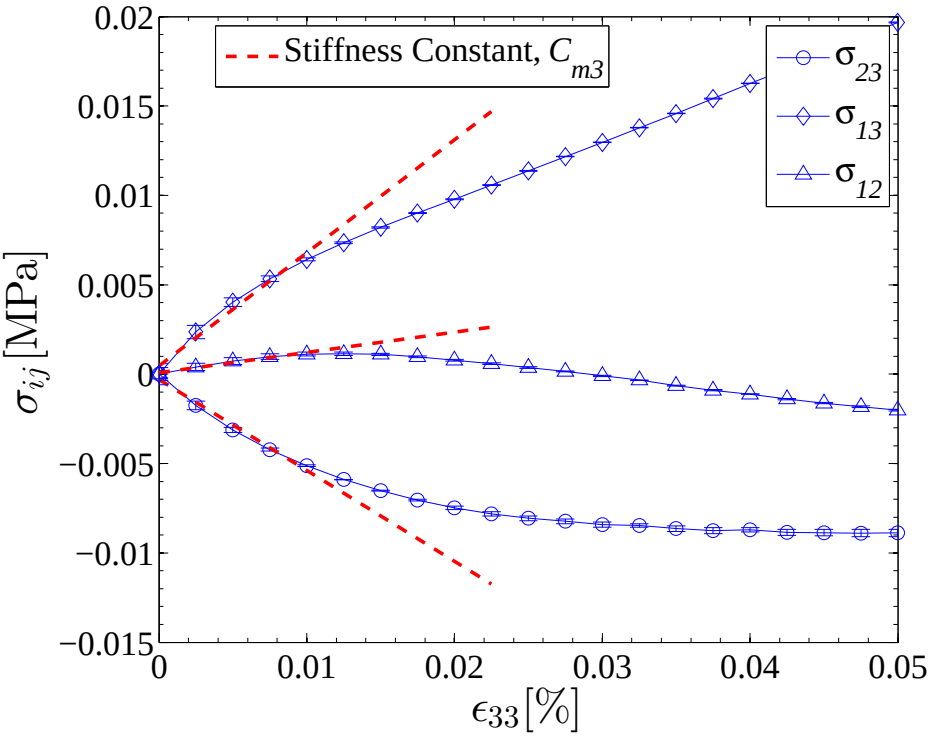
Stiffness Constant, C_{m3}
σ_{23}
σ_{13}
σ_{12}
σ_{ij} [MPa]
ϵ_{33} [%]
0.02
0.015
0.01
0.005
0
−0.005
−0.01
−0.015
0.01
0.02
0.03
0.04
0.05

(b)

Figure 16

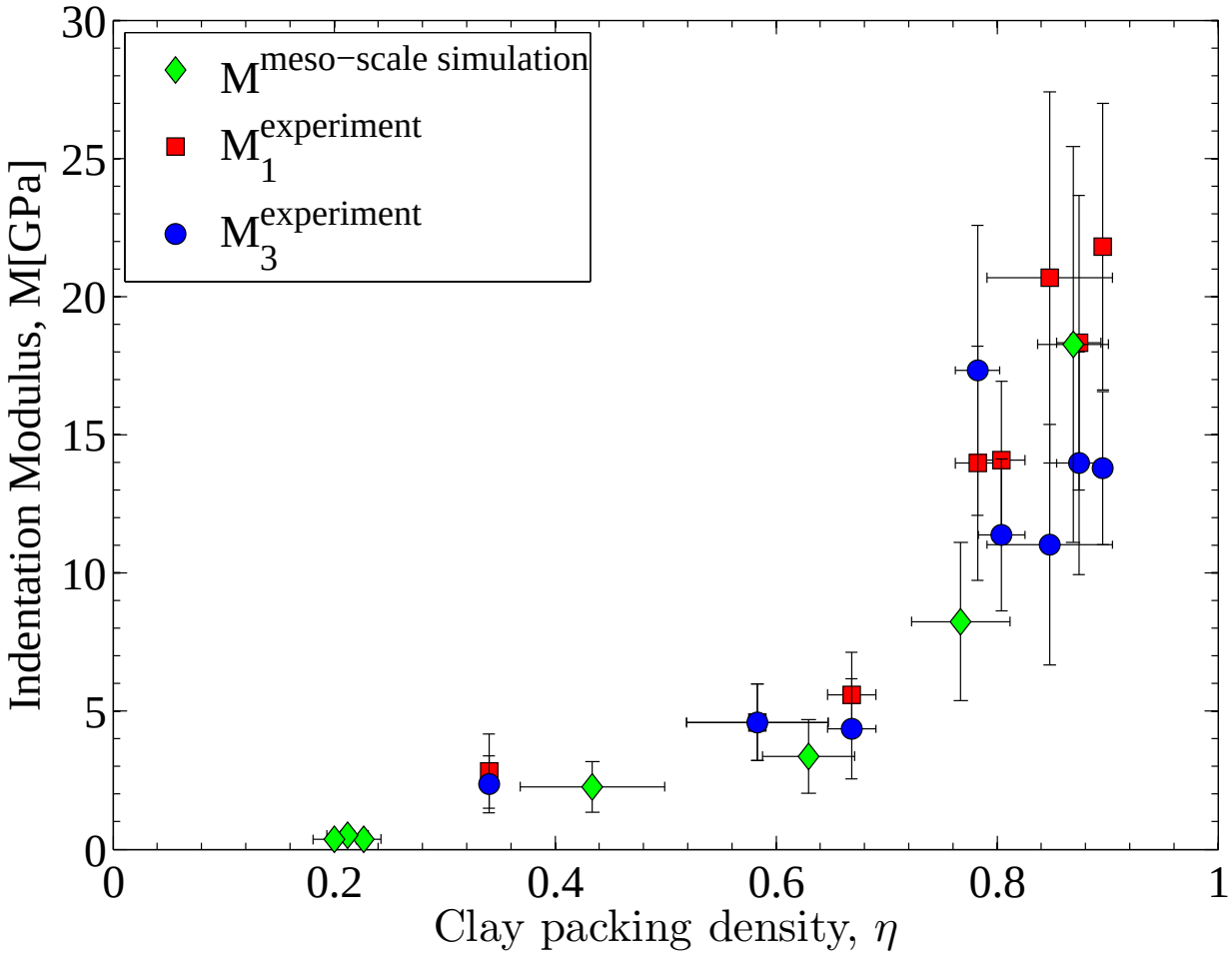
M meso−scale simulation
M1 experiment
M3 experiment
Indentation Modulus, M[GPa]
Clay packing density, η
0
5
10
15
20
25
30
0
0.2
0.4
0.6
0.8
1